Ocean-based heat transfer across the equator in the Arabian Sea over Glacial and Interglacial transitions

Graduation research project for the (sedimentary) Geology Master for 60 ECTS

Student name: Irina Rammos
Student number: 3132129
Supervisors: Gert-Jan Reichart (UU) & Geert-Jan Brummer (NIOZ)
Date of submission: 15 July 2011

Abstract

Keywords*: Arabian Sea, Temperature proxies, XRF scanning, Equatorial heat exchange*

The Asian Monsoon system influences to a great extent the weather of the tropics and subtropics of the eastern hemisphere. Dominant factors that determine the strength of the monsoon are sea surface temperature (SST) and related heat transport across the equator. Since the tropical monsoon causes intra-annual variability in SST, reconstructing the short-term variability in seawater temperature and cross-equatorial heat transport is the only way to understand the development of the monsoon system over time.

The objective of this study is to compare well-known sediment records of the Northern Arabian Sea with the low-latitude Indian Ocean in terms of sediment supply and heat transport during the last glacial-interglacial. Sea surface temperatures (SST) and intra-annual temperature variations can be reconstructed from $\delta^{18}O$ and Mg/Ca of planktic foraminifera. Comparison of the foraminifera-based SST reconstructions of core INATEX-08 with SST reconstructions from the Northern Arabian Sea allows for a detailed reconstruction of glacial-interglacial evolution in heat transfer across the Arabian Sea.

The agemodel of INATEX-08 is constructed using stable oxygen isotopes of the calcite of *G. sacculifer* and the disappearance of Pink *G.ruber*. All $\delta^{18}O$ records were correlated to the composite benthic $\delta^{18}O$ record of Martrat et al., 2007 from the Iberian margin, which enables a good correlation between Southern and Northern cores. Temperature reconstructions of INATEX-08 are based on calcite chemistry of single foraminiferal shells of *G. ruber*. Individual size and weight analyses are performed to test variability of size-normalized weights over time. From the same specimens, Mg/Ca is determined to establish variability in sea surface temperatures. Results are compared to other temperature reconstructions based on 1) the use of similar proxies in different cores and 2) the use of other proxies applied to these cores (U^k_{37} and TEX_{86}).

Detailed variations of sediment composition in INATEX-08 were acquired non-destructively by XRF scanning, showing: 1) Strongly reduced lithogenic concentrations during MIS 6 and slightly reduced concentrations during MIS 4 and the LGM, 2) The last deglacial (around 12kyrs) shows the strongest increase in lithogenic material and highest lithogenic concentrations, 3) Zr/Rb ratios show a strong increase of the coarse-grained lithogenic fraction during the deglacial (12Kyrs) and 4) The high Zr/Rb ratios during the LGM, MIS 4 and MIS 6 suggest a reduction of the lithogenic sand fraction during glacial periods.

A comparison between SST proxies applied to cores from the Southern and Northern Arabian Sea shows that 1) the difference between LGM and Holocene is similar for all cores with a slightly larger difference for INATEX-08 and colder temperatures for NIOP 478, 2) TEX_{86}-based temperature reconstructions result in the largest difference, with warmer average temperature during the interglacial compared to the other proxies, and colder average temperature during the glacial, 3) Mg/Ca-based reconstructions reveal that SST ranges of the Holocene become larger as one moves from the South to the North with the temperature range for NIOP 478 being the largest, 4) TEX_{86} results in higher SST values than obtained using Mg/Ca and U^k_{37}.

Contents

1. Introduction

The Asian Monsoon system is one of the major climate phenomena active today and influences to a great extent the weather of the tropics and subtropics of the eastern hemisphere (Clark et al, 2000). Sea surface temperature (SST) and related heat transport across the equator is thought to be related to the strength of the summer monsoon in the Arabian Sea (Shukla, 1975). Colder SST's result in higher sea surface pressures, less evaporation and hence less cross-equatorial moisture flux (Chowdary et al., 2006), resulting in reduced rainfall (i.e. weaker monsoon).

Seasonality plays a major role in the Arabian Sea and resulting temperature gradients can be much more extreme than annual SST changes. Since temperature extremes due to seasonality reflect differences in winter and summer seasons, reconstructing temperature ranges is of importance to understand development of this weather system over time. Nevertheless, proxies for SST, in particular those based on foraminiferal calcite, are also influenced by other variables (e.g. salinity, carbonate chemistry, symbiont activity and/or ontogenetic effects). Hence, in order to reliably reconstruct seasonality from foraminifera, it is necessary to determine which parameters influence variability in SST recorded by foraminifera. In addition it is of significance to see how much seasonality influences SST extremes and whether the degree of influence changes over the Arabian Sea. Comparison between reconstructed SST ranges from different sites in the Arabian Sea allows investigation of this degree of influence. Also, comparison of temperature ranges obtained by different proxies for SST (U^k_{37}, TEX_{86} and Mg/Ca) may lead to the detection of consistent over- or under estimation by these proxies. Additional proxies are provided by XRF data which are indicative of wind strength, terrestrial input and productivity, all features characteristic of monsoon strength.

This study aims to quantify and understand variability in oceanic heat transfer across the equator in the Arabian Sea over several intervals (Holocene, LGM, MIS4, MIS5e and MIS6). For this purpose, a core from the Southern Arabian Sea along the Tanzanian Margin, INATEX-08, is investigated and compared to core data from northern sites in the Arabian Sea (NIOP 478 and NIOP 463 from the Pakistan margin, and NIOP 905 from the Somali margin) so that the entire latitudinal gradient of the Arabian Sea is covered and the variability of seasonality between North and South can be investigated.

XRF core scanner data will be used for constructing a stratigraphic framework (and allow locating intervals of interest) along the East African margin and the Arabian Sea. In addition XRF core scanning data allows reconstruction of terrigenous input and surface water productivity that can be interpreted as changes in continental climate and surface wind systems. Calcitic Mg/Ca ratios of individual specimens of *Globigerinoides ruber* from INATEX-08, will be used to reconstruct SST and thereby heat transport across the equator. Combined, these data allow reconstruction of variability in SST within the analyzed intervals, analysis of variability in the cross-equatorial heat budget and its relation to monsoon intensity.

In this thesis all the necessary additional information concerning the Arabian monsoon system, and previous knowledge, is discussed in chapter 2. Chapter 3 describes the materials and methods used, followed by the results, (XRF, Size and weight analysis, Mg/Ca measurements and temperature data) in chapter 4. The concluding remarks are summarized in chapter 5.

2. Additional Information

In this chapter the Arabian monsoon system and hydrography will be described in section 2.1. Sections 2.2 and 2.3 are devoted introduction of the XRF scanning and Laser Ablation-ICPMS. Section 2.4 provides and describes previous studies using Mg/Ca as a proxy for seawater temperature.

2.1. Regional Setting

The Monsoon system is characterized by seasonally reversing winds, which are the result of differential heating of land and ocean masses and the movement of the intertropical convergence zone (ITCZ). The ITCZ moves upwards during the summer and downwards during the winter (see white dotted line in figure 1). The south-western wind system of the Asian summer monsoon brings moist winds and precipitation to the Indian continent. In addition, the monsoon winds above the Arabian Sea result in the upwelling of cold (18-22ºC) nutrient-rich waters along the coasts of Somalia and Oman and increased surface water productivity in the Northern Arabian Sea (e.g. Peeters et al., 2002). Since the summer monsoon winds have a greater intensity than the winter monsoon winds, the summer monsoon in characterized by enhanced dust transport into the Arabian Sea. The main sources of this dust are from the deserts and coastal areas of the Arabian Peninsula as well as from the Northern tip of the Persian Gulf near Iraq (Clemens, 1998) . In the winter (see figure 1), winds (with reduced intensity) reverse and dry air is transported from the north-east over the Arabian Sea. Minor upwelling may result from these winds along the coast of India and Pakistan.

Impacts of the monsoon on the productivity and terrigenous input are preserved as chemical signatures in the sediments of the Arabian Sea and can be used to reconstruct the monsoon system over time. Mechanisms that determine intensity of and variability in the monsoon system are poorly understood. Changes in low-latitude solar radiation, ice sheet extent, SST and continental albedo have been suggested to impact the monsoon system. The SST and heat transport over the equator are proposed to have a crucial role in the strength of the summer monsoon (Shukla, 1975). Colder SST results in higher sea surface pressures, less evaporation over the Arabian Sea and hence less cross-equatorial moisture flux (Chowdary et al., 2006). This in turn, results in less rainfall (i.e. a weaker monsoon). Since SST is related to the strength of the monsoon, proxies that record SST, such as foraminiferal calcite, can be used to reconstruct monsoon variability. In addition, elemental concentrations that are typical of terrigenous material, enhanced productivity or wind strength, all being characteristics of monsoon strength, can be interpreted as changes in continental climate and surface wind systems.

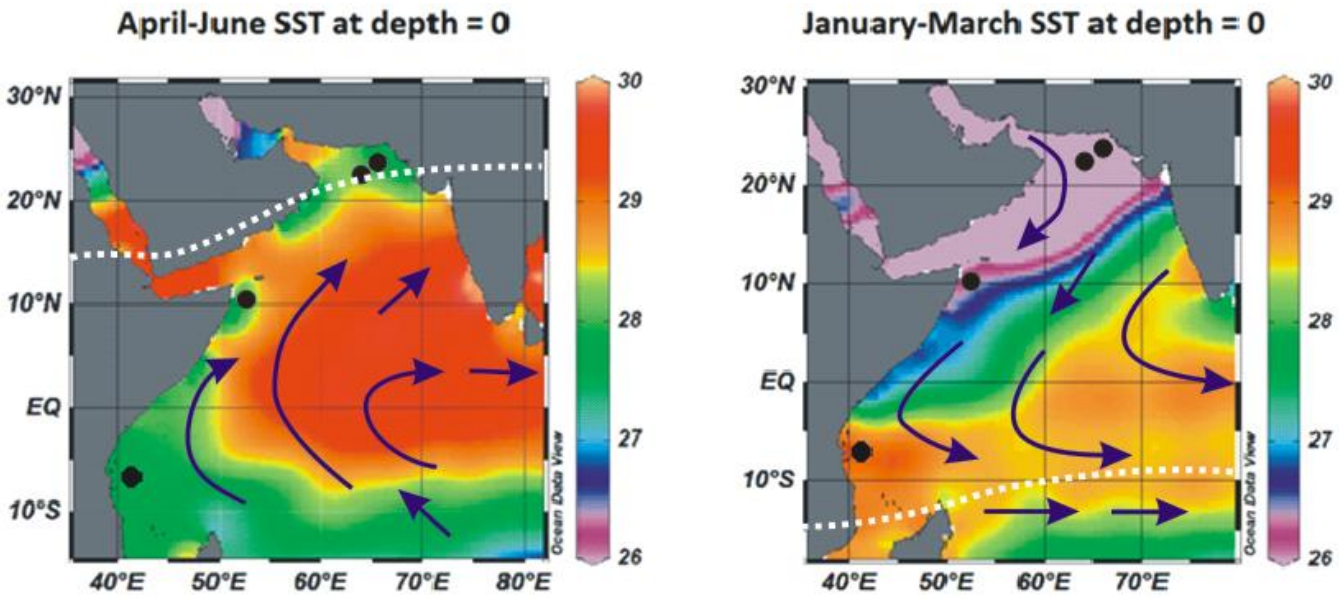

Fig 1) Arabian Sea SST data in the summer months April to June (left) and January to March (right), at depth 0m. (ODV, WOA2009). Pockets of relatively low SST's along the Somalian and Oman coasts indicate upwelling of deeper, colder water due to prevailing southwestern winds. Black dots indicate location of cores (from South to North) INATEX-08, NIOP 905, NIOP 463 and NIOP 478. Arrows indicate wind direction and white dotted lines indicate the position of the ITCZ during the summer and winter monsoon seasons.

Ocean currents play another important role in the North-South heat transport in the Arabian Sea. Surface currents respond to wind direction which changes during winter and summer seasons. These currents cause upwelling of colder waters along the Somali coast and North Arabian Sea during the summer monsoon, and is accompanied by enhanced productivity during this time. Hence, depending on the strength of the wind system (monsoon intensity) the intensity of upwelling and or accompanied productivity is affected, which in turn influences the proxies recording productivity and sea surface temperature. An understanding of the current system in the Arabian sea is thus of importance in interpreting the signal such proxies provide. The main ocean currents in the South-West Arabian Sea, are the South equatorial current (SEC), the East Africa coastal current (EACC) and the Somali current (SC), see figure 2 (Swallow & Fieux, 1991). The SEC flows westwards towards the coast of Tanzania passing Madagascar and splits in the southward directed Mozambique current and the northward directed of the EACC. At the location of INATEX-08 the EACC is the major ocean surface current (figure 2). During the summer monsoon the EACC is fast and merges with the northward flowing SC in the North resulting in cool surface waters and strong mixing deep in the column. During the NE monsoon the EACC moves slower and merges with the southward flowing SC into the equatorial counter current. Less mixing occurs during this time (Mclanahan, 1988).

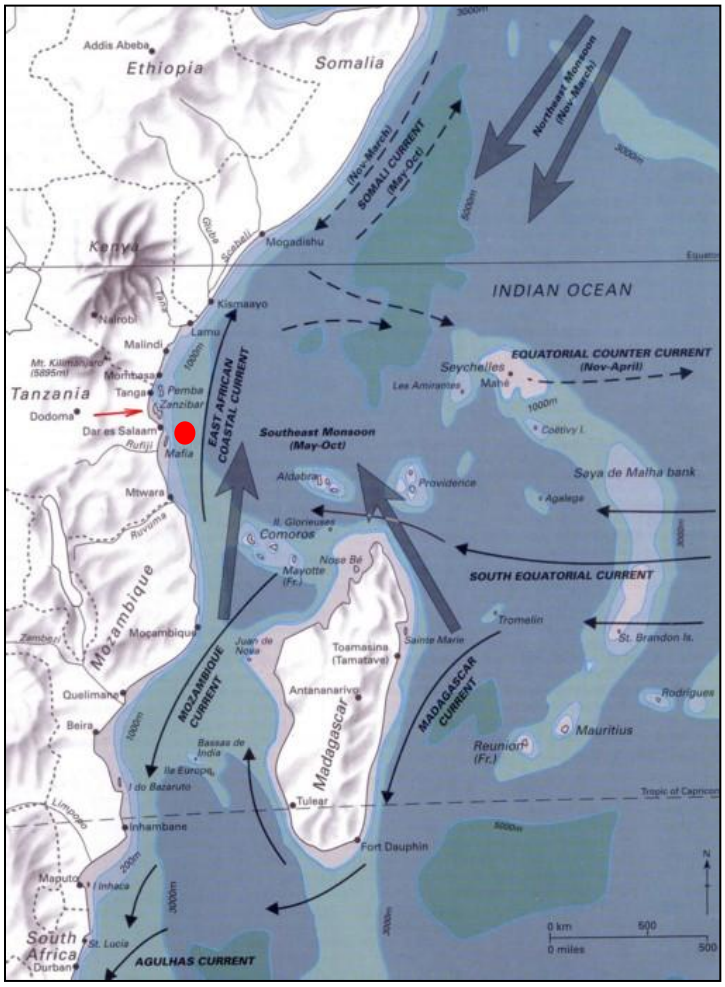

Fig 2) Summary of the major current systems around core INATEX-08 (see red circle). The SEC flows westwards and splits into a northern branch, the EACC and a southward branch, the Mozambique current. Depending on the season the EACC merges with the Northward flowing Somali current during the SW monsoon or merges with the Southward flowing Somali current during the NE monsoon (Richmond, 1997). The red circle indicates the location of INATEX-08.

2.2. XRF scanning

X-Ray Fluorescence (XRF) scanning of sediment core material provides a fast and non-destructive method to analyze the chemical composition of the core material. Second generation *Avaatech* XRF core scanner, currently used in NIOZ (Texel), covers atomic mass ranges from Al to U. Nevertheless, this method has its limitations due to physical properties such as water content, porosity, grainsize differences and surface roughness which may influence the scanner data. Especially lighter elements, such as Al and Si, are affected by water content (Tjallingii et al., 2007). However, a log-ratio calibration (Weltje & Tjallingii, 2008) adequately minimizes bias originating from physical and geometrical irregularities.

The elemental selection will be based on both the geochemical information and the statistical relevance of an element. Previous studies indicated that elements Ca and Sr can be used to indicate changes within marine carbonate production (Richter et al., 2006), whereas Br (Ziegler et al., 2009) and Ba (Jaccard et al., 200X) are related to changes in primary production. Therefore, surface water productivity can be reconstructed by Br/Al. Relative variation of terrigenous input can be revealed by Ca/Ti and Fe/Ca (Arz et al., 1998) and grain-size changes within the terrigenous fraction by using Zr/Rb (e.g. Matthewson et al., 1995).

2.3. LA-ICPMS for Mg/Ca measurements

Since the discovery that foraminiferal Mg/Ca is primarily a function of seawater temperature (Nürnberg et al., 1996) calcitic Mg/Ca has become a popular tool in paleoceanography. Despite intra-shell Mg variability (e.g. Eggins et al., 2003; Sadekov et al., 2005), Mg/Ca of many species can be reliably used to reconstruct SST's. Examples are *Globigerinoides sacculifer Globigerinoides ruber*, *Neogloboquadrina pachyderma* and *Globigerinoides bulloides*. (Nürnberg et al.,1996; Rosenthal, 2000; Sadekov et al., 2008&2009; Dekens et al.,2002; Lea et al., 1999). The error of estimates when reconstructing sea surface temperatures differs depending on the type of calibration made and the species. According to Dekens and colleagues (2002) the error is the least when using *G. ruber* (error of ± 1.2ºC), followed by *G. sacculifer* (error of ± 1.4ºC) and *N. dutertrei* (error of ± 2.4ºC), (see figure 3).

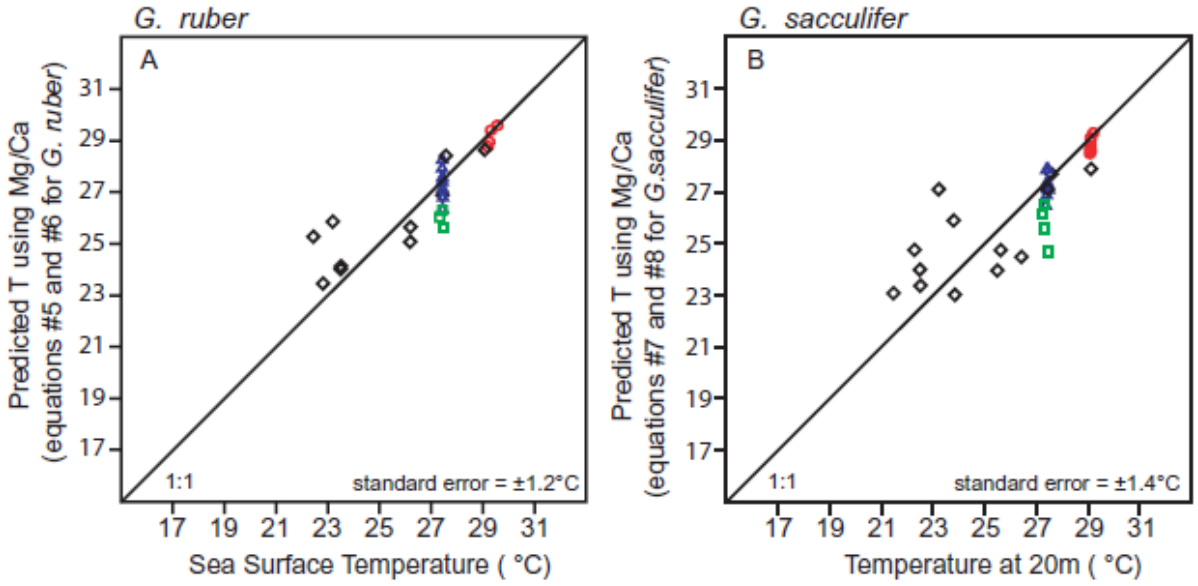

Fig 3) Illustration showing the relation between the SST estimated using Mg/Ca ratios and annual mean SST for species G.ruber (left) and G. sacculifer (right) using species-specific calibrations after applying a correction for dissolution. The standard error for each calibration is shown in the right lower corner, 1.2ºC for G.ruber and 1.4ºC for G. sacculifer (modified after Dekens et al., 2002).

The use of laser ablation-ICP-MS allows accurate determination of Mg/Ca of a very small amount of calcite (e.g. Reichart et al., 2003). This leaves most of a specimen´s calcite for subsequent determination of stable oxygen isotope composition ($\delta^{18}O$)(Anand et al, 2003; Wit et al., 2010).

Since planktic foraminifera have a short lifespan (4-8 weeks, Berger, 1969, Be et al., 1977) Mg/Ca ratios allow for reconstruction of SST's with a very high temporal resolution. Analysis of a large number of specimens from a time interval therefore allows the possibility to reconstruct

the variability (rather than the average) in seawater temperatures (Ganssen et al., 2011). Also, in order to minimize uncertainty of the temperature approximation (to less than 1ºC) at least 20 tests of *G. ruber* are used (Sadekov et al., 2008).

Inaccuracies associated with Mg/Ca-based temperature reconstructions include compositional variation within a population, related to the seasonal cycle or yearly cycles (Eggins et al., 2003). Also, different morphotypes within a species may have significantly different Mg/Ca in case they inhabit different depth habitats and therefore calcify at different temperatures (Sadekov et al., 2008). Thirdly, preferential dissolution and preservation at the seafloor may add to uncertainties (Eggins et al., 2003). Other inaccuracies could be related to biological controls such as depth habitat differences (*G.ruber* lives between 0 and 50m;, Sadekov et al., 2009), upwelling and seasonality (presence throughout the year may vary).

2.4. Background

The use of single-specimen analysis of combined Mg/Ca and $\delta^{18}O$ for paleotemperature reconstructions (Wit et al., 2010) has showed that variability in $\delta^{18}O$ and Mg/Ca of individual specimens mostly covaries with the observed annual temperature variability. This shows that both proxies can be used independently to reconstruct seawater temperature. The differences in temperatures reconstructed from $\delta^{18}O$ and Mg/Ca may be explained by independent responses to salinity, carbonate chemistry, symbiont activity and/or ontogenetic effects (such as differences in growth rate).

Reconstructing seasonality from foraminiferal calcite chemistry is done by the use of species that are dominant in different seasons. Saher et al. (2007) shows that determining the $\delta^{18}O$ and Mg/Ca from specimens of *G.ruber* from core NIOP 929 in the Western Arabian Sea, it is possible to reconstruct the SST for the last 20,000 years. By subtracting the result for *G. ruber* (a species that lives throughout the year) from the $\delta^{18}O$ record of *G. bulloides* (a species that is dominant during upwelling) a new proxy for seasonal SST was tested which was used to reconstruct changes in the strength of the monsoon.

More recently Ganssen et al. (2010) presented Mg/Ca-based SST reconstructions, using foraminifera from box-cores and downcore material. Combining Mg/Ca with $\delta^{18}O$ measurements from single specimens shows a high seasonal range in SST (30 degrees Celcius in spring and 16 degrees during the summer upwelling) off Somalia. Variability in salinity and $\delta^{18}O$ in the upper 200m, on the other hand, were relatively small. Seasonal temperature ranges of the last glacial maximum were shown to be less than those of the Holocene (10.6 compared to 13.1ºC, respectively). Average temperatures range from 28.7 for the Holocene ºC to 26.2 ºC for the last glacial maximum.

Anand et al. (2008) used the same material (i.e. foraminifera from NIOP 905) in combination with another core (SK17), to study past SST and seawater $\delta^{18}O$ variations for the last 35 kyrs.

Using Mg/Ca-derived SST from *G.ruber* and *G.bulloides*, combined with calcitic $\delta^{18}O$ they found that during the last glacial maximum seawater temperatures were 3-4 ºC lower than during the Holocene. They also showed that there was a strong seasonal temperature contrast during the LGM, which may be explained by stronger winter monsoons during glacials and stronger summer monsoons during interstadials.

Huguet et al. (2006) constructed a temperature record of core NIOP 905 using TEX_{86} and U^k_{37} (according to Schouten et al., 2002; figure 4). The U^k_{37} SST record of NIOP 905 displayed minor variability (approximately 1.5ºC) for the last 23kyrs. On the other hand, TEX_{86}-derived temperatures show larger temperature-variability between the LGM and Holocene optimum (from 22-23° to 28-30°C, respectively).

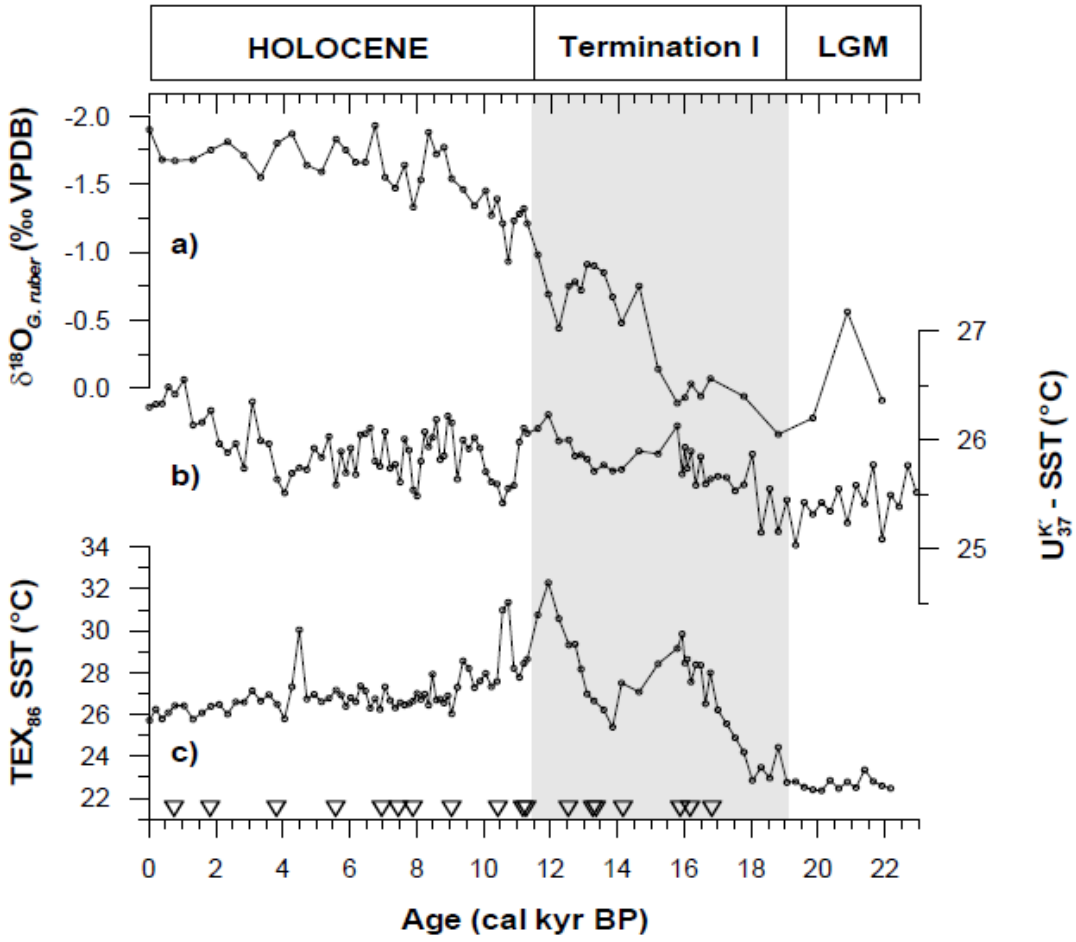

Fig 4) The U^k_{37} and TEX_{86} records for the last 23kyrs for core NIOP 905. Also shown is the G. ruber *δ18O record from Jung et al., 2001 (Huguet et al., 2006). Note the absolute differences in reconstructed temperatures between the proxies.*

3. Methods and Materials

Chapter 3 contains a description of the selected materials (section 3.1) and the methods and preparations conducted for this research (section 3.2). In particular, the preparatory processes of XRF scanning (3.2.1), isolation of foraminifera (3.2.2) and LA-ICPMS (3.2.3) are described. Section 3.3 describes the construction and tuning of the agemodels.

3.1. Materials: Core selection

Several studies showed that both primary production and terrigenous input from the adjacent continents in the Northern Arabian Sea (cores NIOP 905, NIOP 478 and NIOP 463) are closely linked to the monsoonal strength. However, records from the tropical southern Indian Ocean are scarce and climate induced variations of surface water productivity and terrigenous input are largely unknown. INATEX-08, a southern core, is used to gain a better understanding of the relation between primary productivity, terrigenous input and monsoonal strength in the southern Indian Ocean. A comparison with northern cores will provide a better understanding of monsoonal strength and heat transport over the Arabian Sea.

All sediment cores (Table 1) are under direct influence of the Inter-Tropical Convergence Zone (ITCZ) (figure 5). The selected cores cover a large latitudinal gradient and are located in an area that experiences large inter-seasonal variability in wind direction, currents and ITCZ.

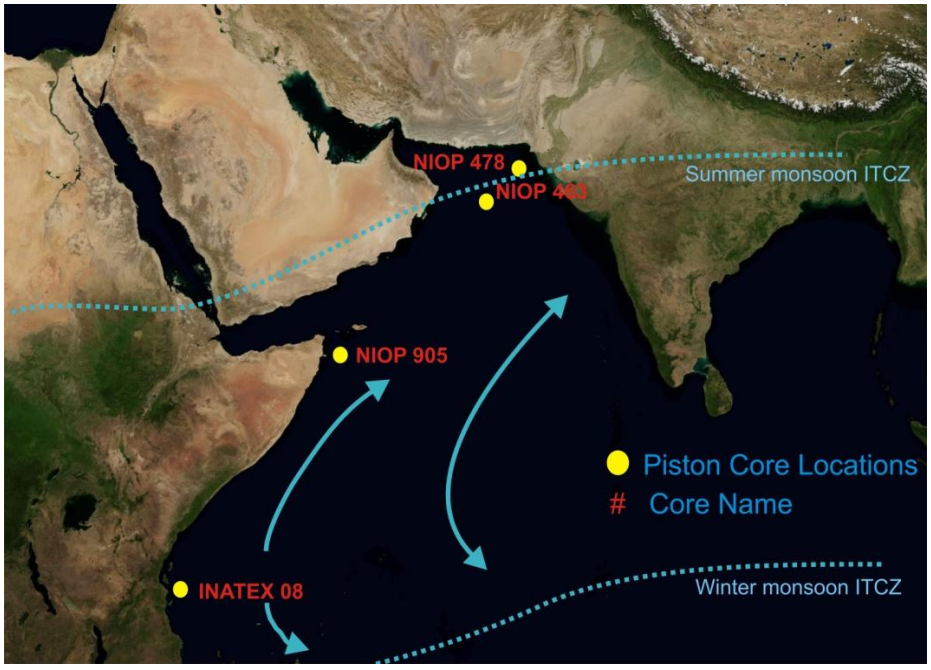

Fig 5) Satellite image of the Arabian Sea with the position of the cores and approximate location of the winter and summer ITCZ.

INATEX 08 was retrieved offshore Tanzania during the "Indian-Atlantic exchange in present and past climate project" of 2009 from a depth of 752m. This core is 6.825m long and consist of

foram-bearing sandy mud (www.nioz.nl, from Corebase database). Northern cores NIOP 463, NIOP 478 and NIOP 905 were all collected during the Netherlands Indian Ocean Programme of 1992/1993. NIOP 463 was retrieved from the Murray Ridge (North Arabian Sea) from a depth of 920m within the present day oxygen minimum zone. Core NIOP 463 has a length of 14.30m and consists mainly of dark green to light grey hemipelagic muds (Reichart et al., 1997). NIOP 478 was retrieved offshore Pakistan from a depth of 565m also within the present day oxygen minimum zone. It has a length of 14.50m and consists of dark-greenish to light-greenish/gray hemipelagic muds with several laminated intervals (Reichart et al., 2004). Core NIOP 905 was retrieved Offshore Somalia (on the continental slope) from a depth of 1586m and below the present day oxygen minimum zone. It has a length of 15.26m and consists of bioturbated calcareous ooze (Ivanova, 2000). Figure 6 depicts the bathymetric location of the cores.

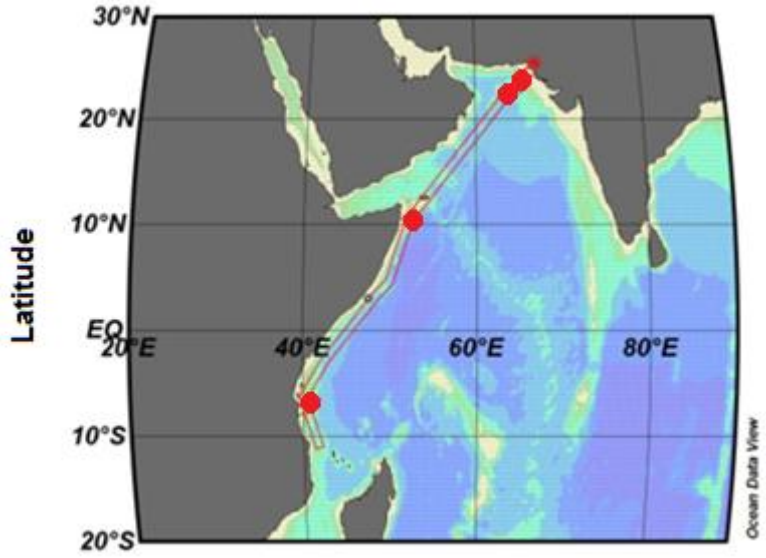

Fig 6) Trajectory within the Indian Ocean (t left) that is used to create a map of the depth spanning the location of the selected cores(red dots in top panel). The resulting bathymetric profile (lower panel) also shows today's oxygen concentration. Note that NIOP 463and NIOP 478 are within the oxygen minimum zone whereas NIOP905 and INATEX 8 are just below it (WOCE Global Hydrographic Climatology, Gouretski & Koltermann 2004 and Ocean data View, available at http://odv.awi.de/).

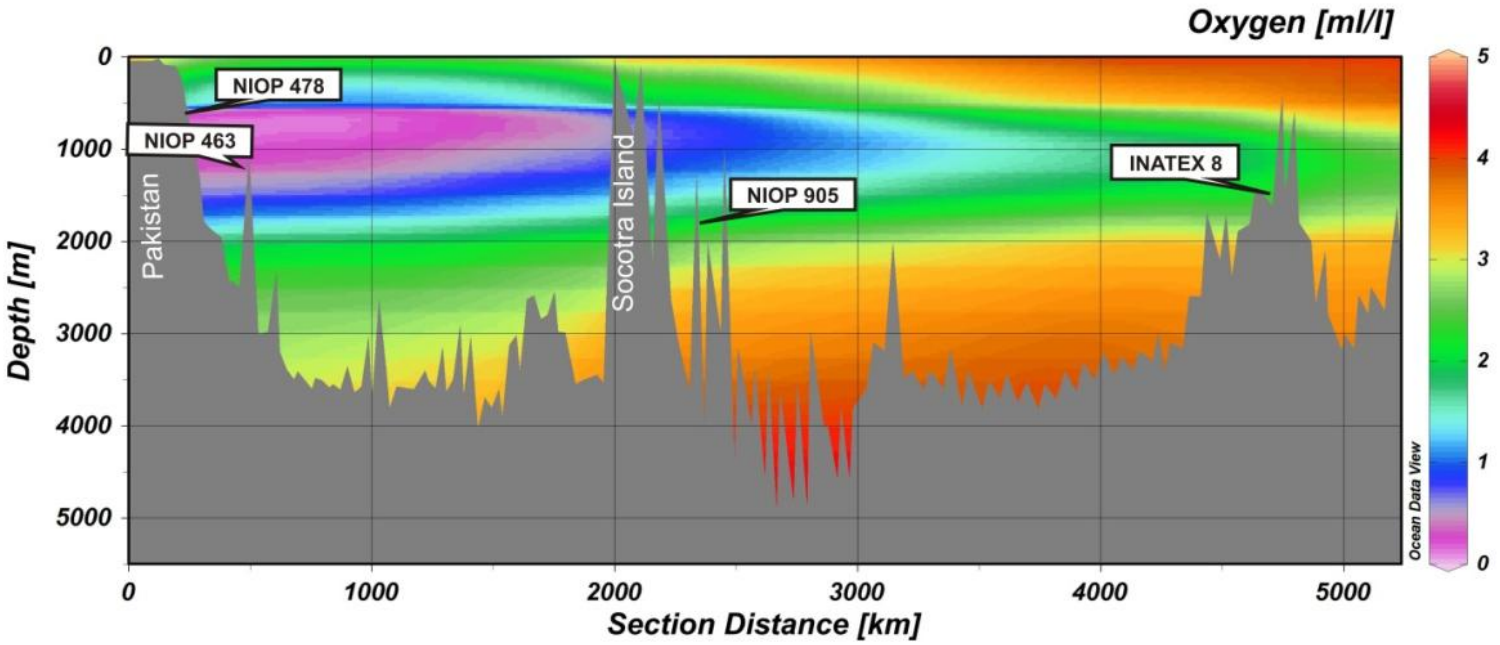

Core Name	Latitude (ºN)	Longitude (ºE)	Water depth (m)	Core Length (cm)
NIOP 478	24.12	65.39	565	1450
PE304-08PC/ INATEX-08	-8.94	39.66	752	682.5
NIOP 905 (TY93-905PC)	10.77	51.95	1586	1526
NIOP 463	22.32	64.02	920	1430

Table 1: Details of the selected cores.

3.2. Methods

3.2.1. XRF scanning

Prior to sampling, all cores were first scanned using the AVAATECH XRF core-scanner to determine elemental composition of the material. XRF data from cores NIOP 463 and INATEX-08 are available from previous studies (both conducted with a resolution of 1 cm). NIOP 478 and NIOP 905 underwent XRF scanning at a spacing of 1 cm for NIOP 478 and 0.5 cm for NIOP 905 (due to the uneven surface of the available half of the core). All cores were scanned at 10 kV and 30 kV so that most atomic mass ranges were covered. In the process of scanning each split core surface was covered by a 4µm thin SPEXCertiPrep Ultralene foil so as to avoid contamination and to protect the beryllium triangle of the XRF corescanner.

3.2.2. Foraminifera Preparation

Core INATEX-08 was subsampled for foraminifera by addition of distilled water to sampled sediments. After 24 hours, samples were sieved over a 63 µm-screen and rinsed with ethanol. The residue dried in an evaporation chamber. Dry samples were sieved again at 150 µm and rinsed with ethanol and left to dry in the evaporation chamber.

From the sieved samples of INATEX-8 samples from 5 timeslices were selected: 21 samples from the Holocene, and 4 samples for each of the following: the LGM, MIS 4, MIS 5e, and MIS 6 (figure 7). For each sample, 20 specimens of both *G. sacculifer* and *G. ruber* (sensu strictu) were handpicked using a binocular. Specimens of *G. sacculifer* were crushed between two glass plates and then cleaned twice with distilled water and once with ethanol and then left to dry upon further processing. Crushed *G. sacculifer* samples were weighed using a Santorius scale (error = ± 1 µg) and placed in a mass spectrometer (Finnigan MAT 253) to determine the δ^{18}Ocalcite of the core (figure 6). Specimens of *G. ruber* were used for geochemical analysis (i.e. Mg/Ca) using laser ablation-ICP-MS (see section 4.2.3).

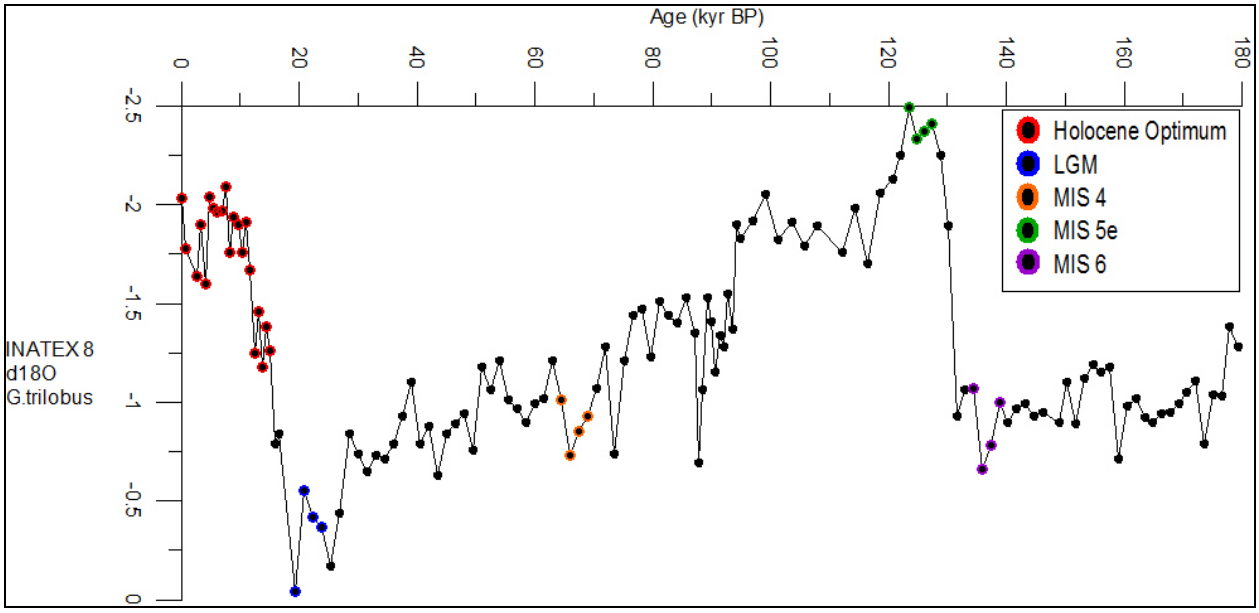

Fig 7) Oxygen isotope record of core INATEX-8 using G. sacculifer. *Differently colored samples indicate samples used to determine Mg/Ca by laser ablation.*

An additional stratigraphic marker, the timing of the disappearance of pink *G. ruber*, is determined to independently validate the constructed agemodel. Since pink *G. ruber*s are known to disappear at MIS event 5c (120kyr BP) in the Indo-Pacific oceans, its abundance in INATEX8 can be used to accurately time this event (Thompson et al., 1979). For all samples, 300 individuals of *G. ruber* (white and pink), greater than 150µm were counted to determine the relative abundance of pink *G.ruber (p/p+w*100)*.

3.2.3. Size-normalized weights and Laser Ablation-ICP-MS

For determination of the single-specimen Mg/Ca by Laser Ablation-Inductively Coupled-Mass Spectrometry (LA-ICP-MS) specimens of *G. ruber* from five intervals were isolated (see figure 7). Prior to analysis, individual specimens were weighed using a Santorius scale (error = ± 1µg) and their size was determined according to Beer et. al. (2010) where the length from the top chamber to the depression between the two lower chambers on the apertural side is determined (figure 8). Size analysis was performed using image analysis software from Leica Microsystems (Leica Application Suite V 3.1.0)

Combined weights and sizes from all specimens allows determination of single-specimen size-normalized weights. For every sample, 20 specimens were thus processed and the average SNW of these 20 specimens is determined. In addition the last chamber is used for laser ablation since less Mg/Ca rich layers and little Mg/Ca variation is expected here due to migration within the water column (Sadekov et al., 2009).

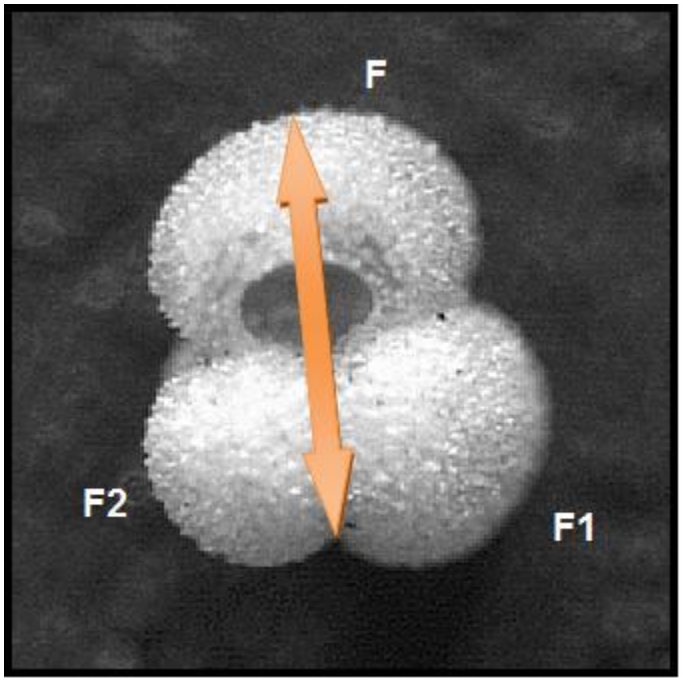

Fig 8) Example of a size measurement in G. ruber. *Final chamber (F), penultimate (F-1) and pre-penultimate chamber (F-2) are indicated. All specimens were placed so that the aperture is visible and parallel to the surface they are placed on. Size of each specimen is determined by the length between the depression between the F-1 and F-2 chambers and the tip of the F-chamber. For example, a specimen with a size of 0.363mm and a weight of 0.016mg has a SNW of 0.363/0.016=22.69 mm/mg.*

Prior to LA-ICP-MS measurements, specimens of *G. ruber* were cleaned to remove clay particles, detrital and diagenetic phases. Different methods were tested in order to optimize the cleaning protocol. The method provided by Barker et al. (2003) and two modifications of this protocol were tested on a similar-sized group of specimens (table 2).

	Method		
	Barker et. al. 2003	Modified method 1	Modified method 2
Description	3X Milli Q, 2x Methanol, 3X Milli Q, 10sec in sonic bath after each step	3X Milli Q, 2x Methanol, 3X Milli Q, 1sec in sonic bath after each step	3X Milli Q, 2x Methanol, 3X Milli Q, 4 sec in sonic bath after 2nd time Milli Q and 1st time Methanol
Comments	Clean but 68.7% shattered	Not clean enough and 26% shattered	clean but 13.9% shattered

Table 2) Description of the methods tested for cleaning G.ruber prior to Laser Ablation.

The first cleaning protocol resulted in mechanical destruction of more than 30% of the number of foraminifera treated (table 2). The first alternative method involved decreasing the sonic bath time of the foraminifera from 10 seconds to 1 second. This resulted in a destruction of about 26%

of the specimens, although subsequent analysis showed remains of contaminant phases (figure 8). The second alternative protocol involved placing specimens within the sonic bath only twice for 4 seconds (once after the second MilliQ addition and once after the first Methanol addition). The latter method proved to be the least destructive (13.9%) and the samples are clean enough for use in the LA-ICPMS. Figure 9 shows the three methods used, and degree of contamination (Al/Mn contents). Comparison to uncleaned specimens allows quantification of the efficiency of the different cleaning protocols.

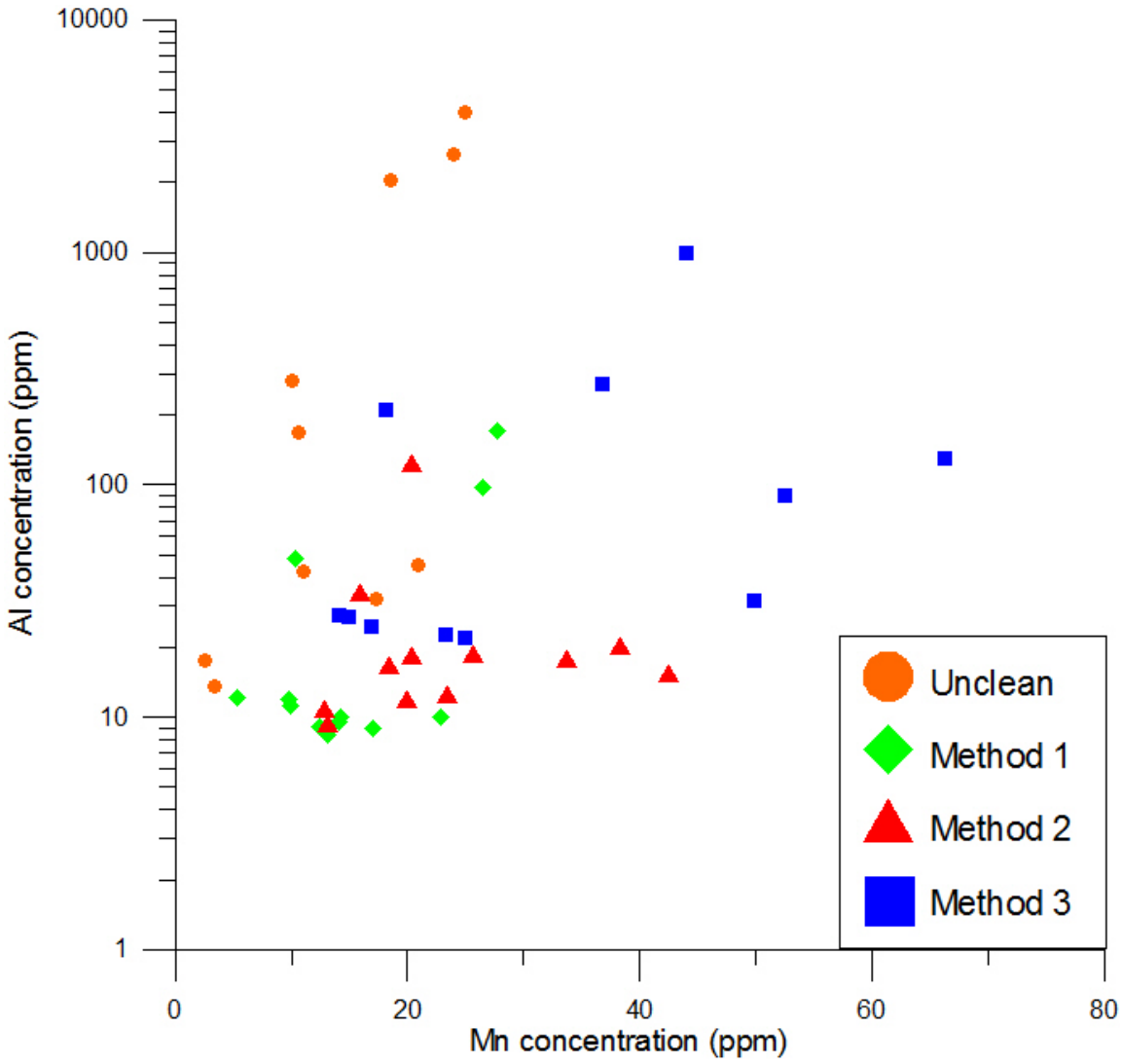

Fig 9) Contamination indicated by Al (logarithmic) versus Mn concentrations for the three tested methods and uncleaned specimens. Removal of contamination were highest by modified method 1 and modified method 2. Since modified method 2 proved to be the least destructive, this is the method used for the remaining foraminifera.

The laser (Lambda Physik Lasertechnik COMPEX) is connected to an Element2 Mass Spectrometer (Thermo Scientific) for the determination of elemental composition of the

foraminiferal calcite. Ablation crater diameter was set to 80 µm, energy density to 1 J/ cm^2 and pulse rate to 7 Hz. Before and after every ~12 samples, a glass standard N610 (NIST) was ablated three times with a higher energy density (~5 J/ cm^2) as an external standard (Pearce et al., 1997). An Iceland spar calcite (GJR) was ablated 3 times after ~12 samples too and served as a matrix-matched standard. ^{43}Ca was used as an internal standard, assuming 40% wt in the foraminifer's and external calcite's standard. Other masses that were measured include ^{24}Mg, ^{26}Mg, ^{27}Al, ^{44}Ca, ^{53}Mn and ^{88}Sr. After ablation, a number of specimens were photographed using scanning electron microscopy (SEM) to determine the quality of the ablation craters and detection of surface structures of the foraminifera (figure 10).

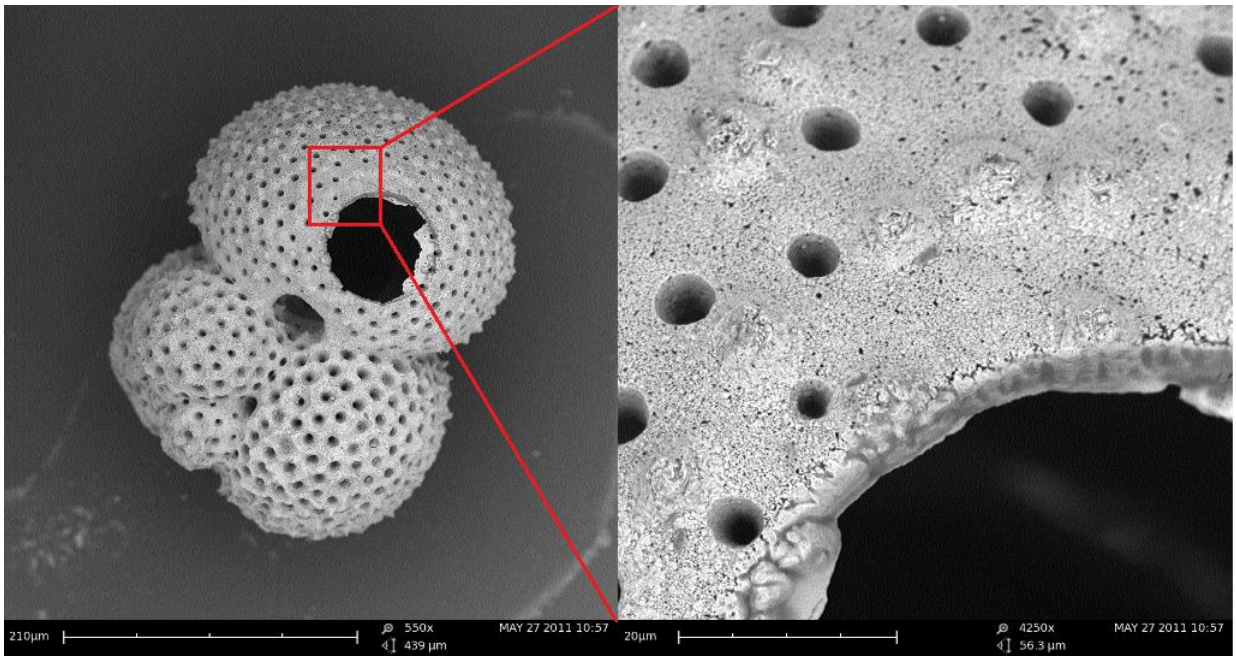

Fig 10) SEM image of an ablated specimen of G. ruber *from MIS 5e (INATEX-8). All measurements spanned ablation of the complete chamber wall.*

All resulting ablation profiles (see for example figure 11) were integrated with the Glitter software (Gemoc) to select the background, sample and detect contaminations. The latter is based on presence of relatively high amounts of Al and/or Mn. The selected, contamination-free measurement is used to determine average Mg and Ca concentrations (figure 11).

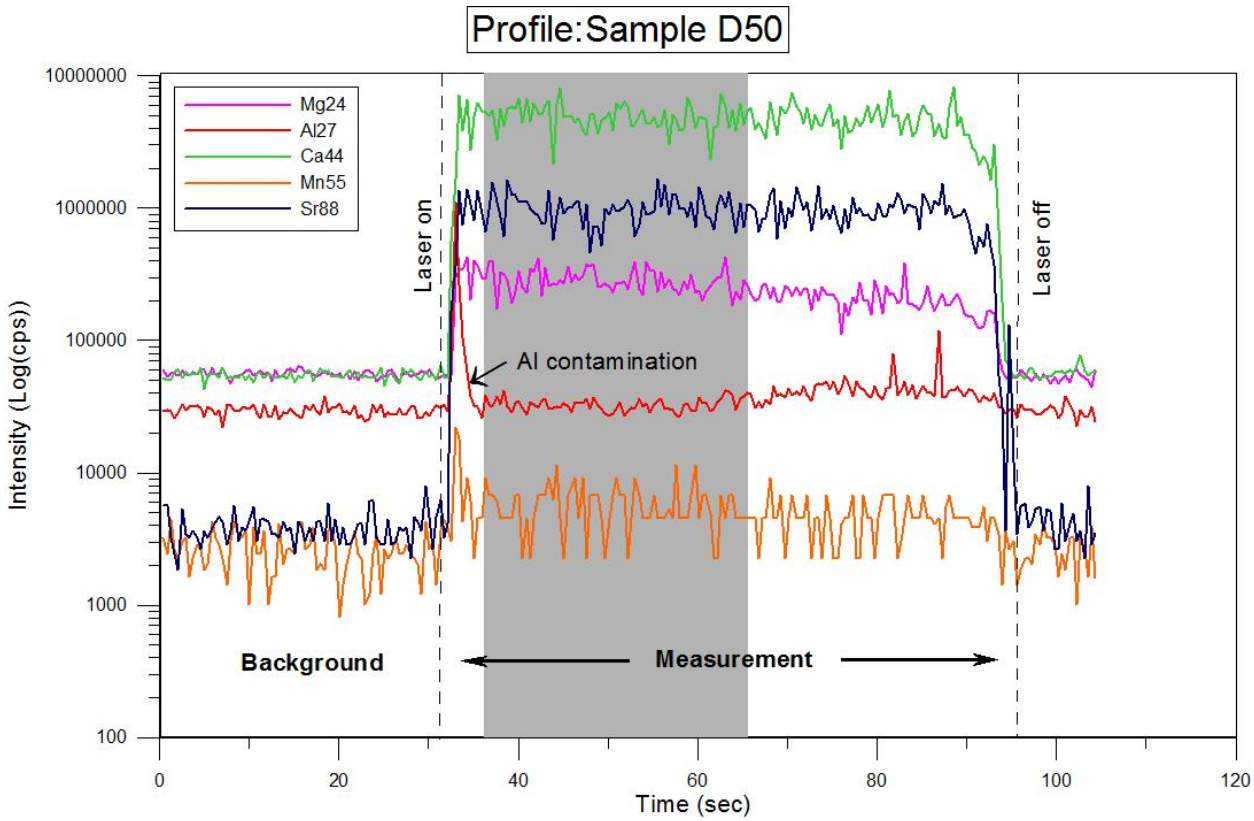

Fig 11) Example of a Laser Ablation-ICP-MS profile (sample D50, LGM). Magnesium and Calcium profiles are shown with pink and green respectively. The grey area depicts the selection made on basis of the Al and Mn profiles indicating contamination on the outer and inner surfaces of the chamber wall; note the Al peak on the outside of the chamber wall (left side) and an increase of Al levels towards the inner side of the chamber wall.

3.3. Agemodel for INATEX-08

The agemodel for INATEX-08 is established using a stable oxygen isotope record from *G. sacculifer*. This record was correlated to the composite core record of benthic $\delta^{18}O$ in cores MD95-2042 and MD01-2443 from the Iberian margin (Martrat et al., 2007). MD95-2042 is used for the first climate cycle and MD01-2443 is used for climate cycles 2 to 4. See figure 12 for the correlation points used, the correlation coefficient is 0.855. Also, the independent stratigraphic marker, the disappearance of pink *G. ruber*, is determined to be at a depth of about 469cm, corresponding to an age of ~120 kyrs according to the constructed agemodel, hence validating the agemodel (figure 12).

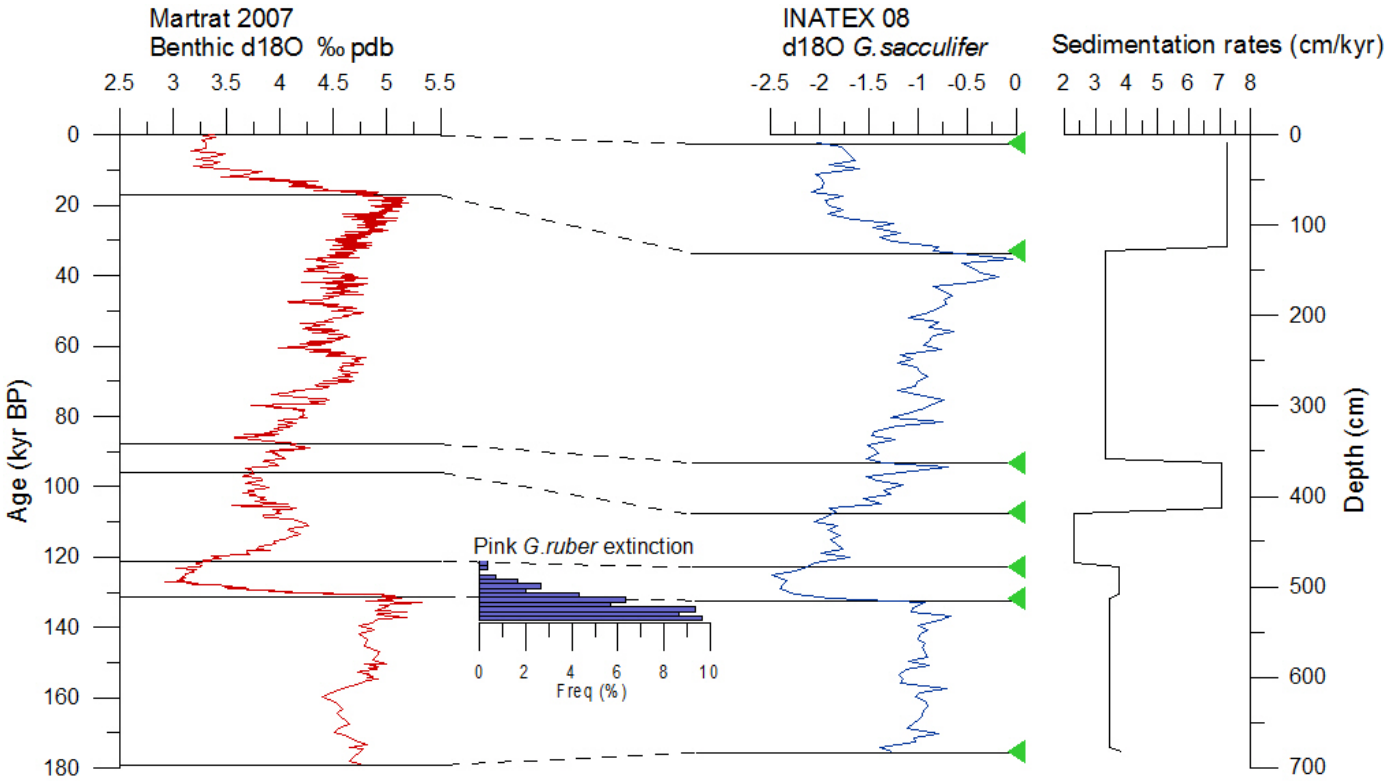

Fig 12) Selection of points used to construct an agemodel for INATEX 8 (green triangles). Left is shown the composite benthic $\delta^{18}O$ record from Martrat (2007), middle is shown the $\delta^{18}0$ record of INATEX08 against depth using G. sacculifer, *right are shownn the sedimentation rates. Relative abundance of pink* G. ruber *in INATEX-08 is also shown as a histogram in the middle. Disappearance of pink* G. ruber *occurs around depth 469, corresponding to an age of ~120 kyrs.*

For the remaining cores (NIOP 905, NIOP 463 and NIOP 478) age calibration points are used from previous studies, and correlated to the Martrat (2007) record (figure 13) to facilitate comparison between cores (correlation coefficients with Martrat record are r = 0.930 for NIOP 478, r = 0.903 for NIOP 905 and r = 0.856 for NIOP 463). Correlation analyses were performed using the software AnalySeries (Paillard et al., 1996). The base of INATEX-08 lies at approximately 180kyrs and thus spans the Holocene, LGM, MIS event 4, 5e (Eemian interglacial) and 6. The sedimentation rates of INATEX-08 range between 2.3 cm/kyr between 94-115kyrs to 7.2 cm/kyr during the Holocene.

The agemodel of core NIOP 478 is made using an oxygen isotope record and ^{14}C dates from Reichart et al. (1998). For core NIOP 463 the agemodel is constructed using a linear interpolation between events of the $\delta^{18}O$ record to an orbitally tuned $\delta^{18}O$ record (Reichart et al., 1998). In addition two AMS ^{14}C dates from the coretop are used, which are calibrated to a Th/U timescale (Bard et al., 1990). Core NIOP 463 spans two glacial cycles and has its base at

approximately 205kyrs. It includes the LGM, MIS 4, 5e and MIS 6. The sedimentation rates of this core lie between 3.4 and 17.6 cm/kyr (Den Dulk, 2000). For core NIOP 905 the agemodel is constructed using 12 AMS ^{14}C dates using G.ruber (Ivanova 1999; 2000). An additional 19 AMS ^{14}C datings from mixed planktic foraminifera are also used (Huguet et al., 2006). The base of core NIOP 905 is at approximately 90kyrs (Jung et al., 2009) and includes the Holocene, LGM and MIS 4. The average sedimentation rates for this core in the last 31 kyrs is about 19cm/kyr, reaching up to 36cm/kyr during the Holocene (Jung et al., 2001).

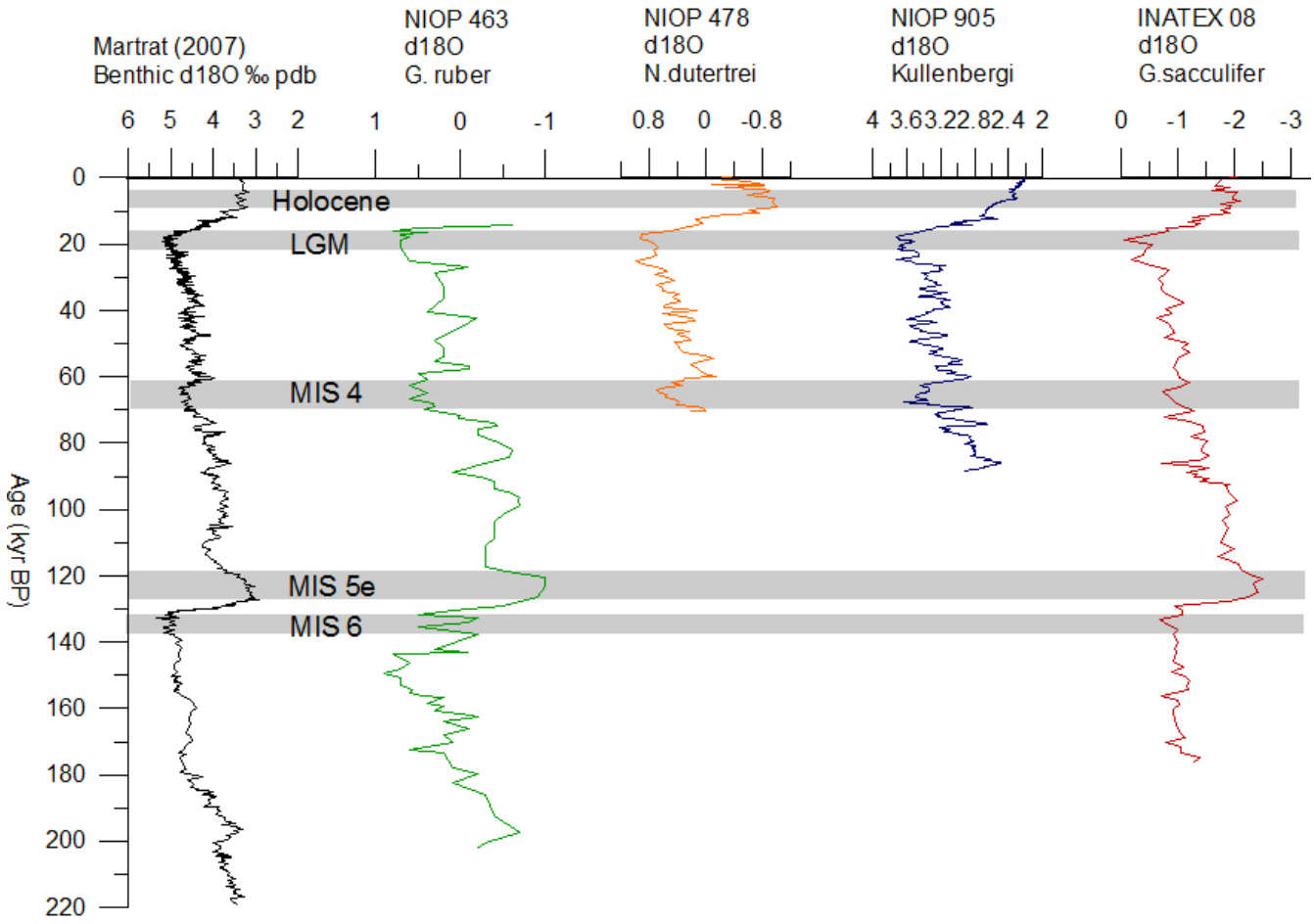

Fig 13) NIOP 463, NIOP 478, NIOP 905 and INATEX-08 correlated to the Martrat composite core of 2007 (far left). The shaded areas depict the timeslices used for this study, from top to base: Holocene Optimum, LGM, MIS 4, MIS 5e and MIS 6.

4. Results and Discussions

This chapter presents the results of the XRF scanning of INATEX-08 (4.1) followed by the results of the foraminiferal size and weight analyses (4.2) and the Mg/Ca results of INATEX-08 (4.3). Finally, the results will be placed in context by comparison of XRF data (4.4) and comparison of SST reconstructions using different proxies and cores (4.5).

4.1. XRF results

Element intensities measured with the XRF core scanner can best be expressed as elemental ratios to minimize the effects of down-core changes of physical properties or sample geometry. Relative changes in the bulk lithogenic material are represented by Ca/Ti, whereas Zr/Rb is related to variations in coarse (> 63μm) lithogenic material. The element Zr is restricted to heavy and resistant zircon minerals with similar transport properties as the silicate sand fraction, whereas Rb is most abundant in the silt and clay fraction (Matthewson et al., 1995). As has been shown by Ziegler et al. (2007) Br concentrations are directly related to marine organic matter, therefore Br/Ti is used as a proxy for productivity.

In addition, Sr/Ca was compared with size normalized weights of foram shells in core INATEX-08 as a possible proxy for carbonate preservation. Both Sr and Ca have long residence times (5 Myrs and 1 Myrs respectively; Martin et al., 1999) and are very little impacted by biological cycling in the oceans. Hence the variability of Sr/Ca on short (glacial-interglacial) timescales should be mostly attributed to environmental and diagenetic parameters (Martin et al., 1999). However, Martin and colleagues (1999) show that the major variations of Sr/Ca of foraminiferal calcite is mostly explained by changes in mean ocean Sr/Ca and correlate to glacial interglacial cycling (related to preferential release of Sr during weathering of shelf carbonates due to changes in sea level). Lesser variations in foraminiferal Sr/Ca are due to the influence of dissolution, temperature, salinity and pH. In fact, live culturing experiments (Lea et al., 1999) show that higher temperature, salinity and pH increase Sr/Ca in planktonic foraminiferal calcite.

Relative bulk lithogenic variations in INATEX-08 are indicated by Ca/Ti ratios that are strongly reduced during the glacial condition of MIS 6 and slightly reduced concentrations during MIS 4 and the LGM (figure 14). The strongest increase in lithogenic material and highest lithogenic concentrations occurred during the last deglacial, around 12 kyr. Variations of the coarse lithogenic grain size indicated by Zr/Rb ratios show a strong increase of the coarse-grained lithogenic fraction during this period (12Kyrs). The high Zr/Rb ratios during the LGM, MIS 4 and MIS 6 suggest a reduction of the lithogenic sand fraction during glacial periods. The relative lithogenic variations indicated by the Ca/Ti ratio and variations of the lithogenic grain-size suggest that higher lithogenic concentrations are related with an increase in the lithogenic sand fraction. The lithogenic sediment supply off Tanzania is probably dominated by fluvial input, although ocean currents could affect sediment transport at this relatively shallow core position as well. A reduced sand fraction during glacials could suggest a less intense EACC during glacials. This implies a stronger winter monsoon (in which the EACC is weaker) and a weaker summer

monsoon (during which the EACC is strong) during glacials. Windblown dust does reach this region but from only a minor part of the total lithogenic input.

Finally the Br/Ti curve shows an increase starting from about 60kyrs to present (figure 14). According to Ziegler et al. (2009) the bromine abundances depend on the amount of marine organic matter as well as terrestrial organic matter which is relatively depleted in bromine compared to marine organic matter. It is unlikely that he increasing trend in INATEX 8 for the last 60kyrs is only explained by high amounts of marine organic matter (i.e high productivity rates). Other still unidentified factors may have played a role in causing this trend.

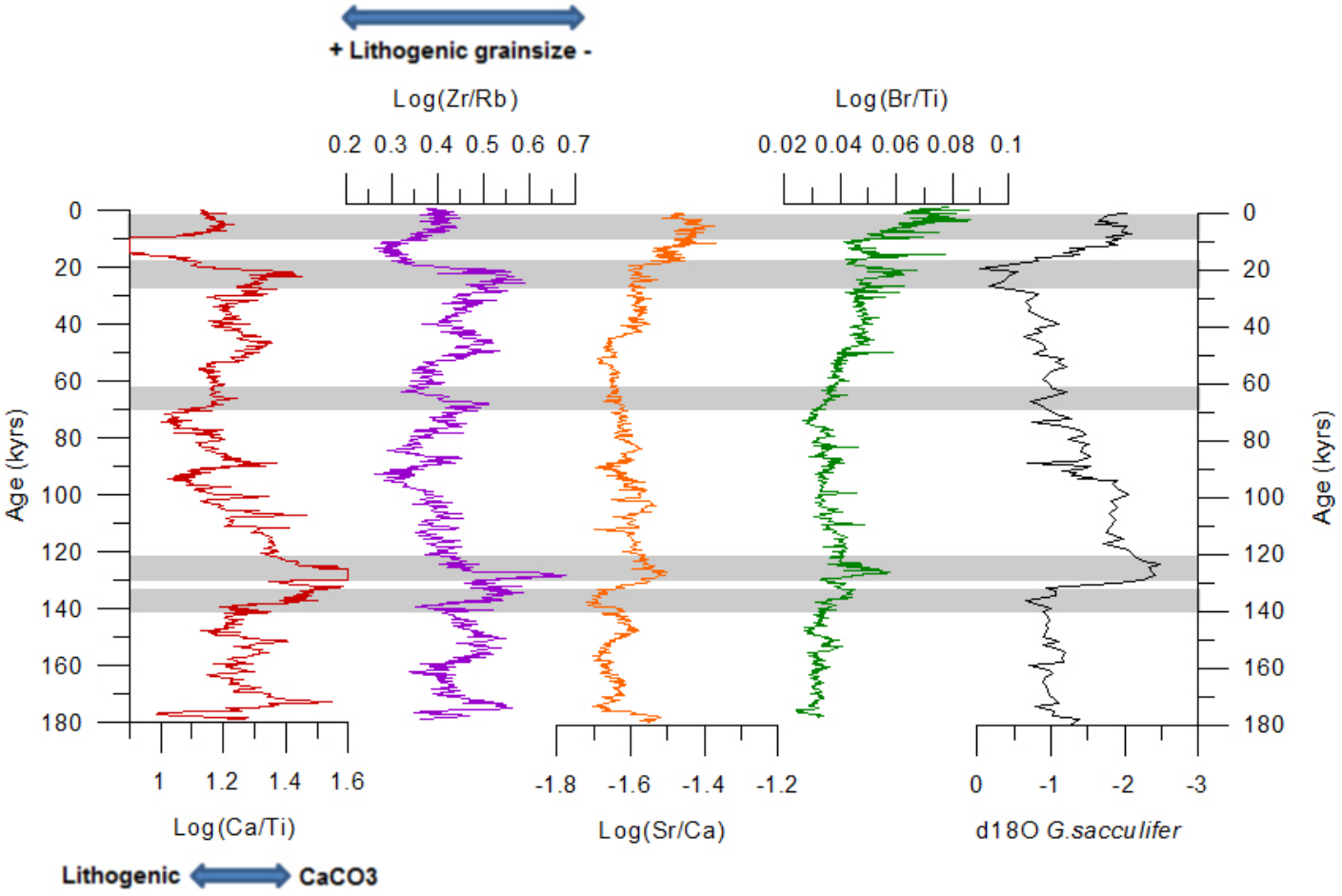

Fig 14) XRF results presented as log ratios for core INATEX 8. The oxygen isotope record based on calcite of G. sacculifer *is added on the right. Grey areas denote the intervals investigated (Holocene, LGM, MSI 4, MIS 5e and MIS 6).*

In INATEX-08 the Zr/Rb ratios show significant variability over time. Perhaps this variability is also seen in the Northern cores. To test whether obliquity and or precession influence this trend in a similar way to the Northern cores the Zr/Rb ratios are compared to the obliquity and precession insolation curves (Laskar, 1990). Figure 15 shows that minima in lithogenic grainsize

correlate to obliquity maxima at around 170 kyrs and 130 kyrs (which is the deglacial period after MIS 6). From around 70kyrs the lithogenic grainsize is dominated by the precession cycle. The strong increase of the coarse-grained lithogenic fraction during the deglacial period (at 12kyrs) correlates well to a precession minima. The high Zr/Rb ratios during the LGM and MIS 4 correlate to precession maxima whereas the high Zr/Rb ratios during MIS 6 correlates to an obliquity maximum.

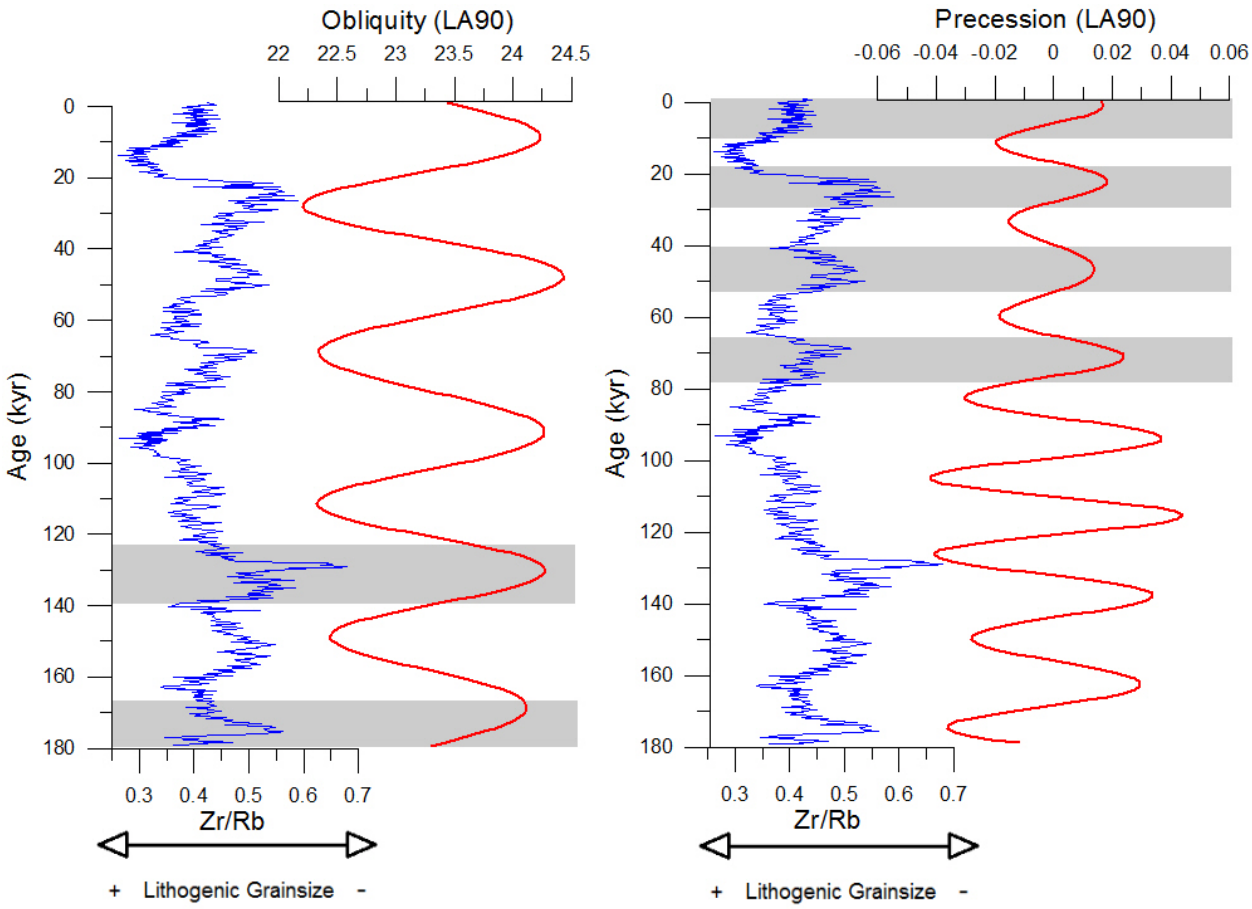

Fig 15) A comparison between the Zr/Rb curve and obliquity (left) and precession(right) curves. The grey areas denote correlations in Zr/Rb peaks and obliquity or precession maxima. The Obliquity and precession curves are from the astronomical solution from Laskar, 1990.

4.2. Size and Weight Analysis

Size-normalized weights (SNW) are larger in foraminifera from the Holocene and MIS 5e (on average ~29 and 30 mm/mg respectively compared to ~27 for the LGM and MIS 4, and 25.3 for MIS 6). In addition, specimens from colder periods, LGM, MIS 4 and MIS 6, have lower minimum SNW's than those from the Holocene and MIS 5e (21 and 23.5 compared to ~ 25 for the Holocene and MIS 5e). Warmer periods thus produce foraminifera with thinner or less dense shells (which can be related to the pore-density) compared to colder periods (figure 16).

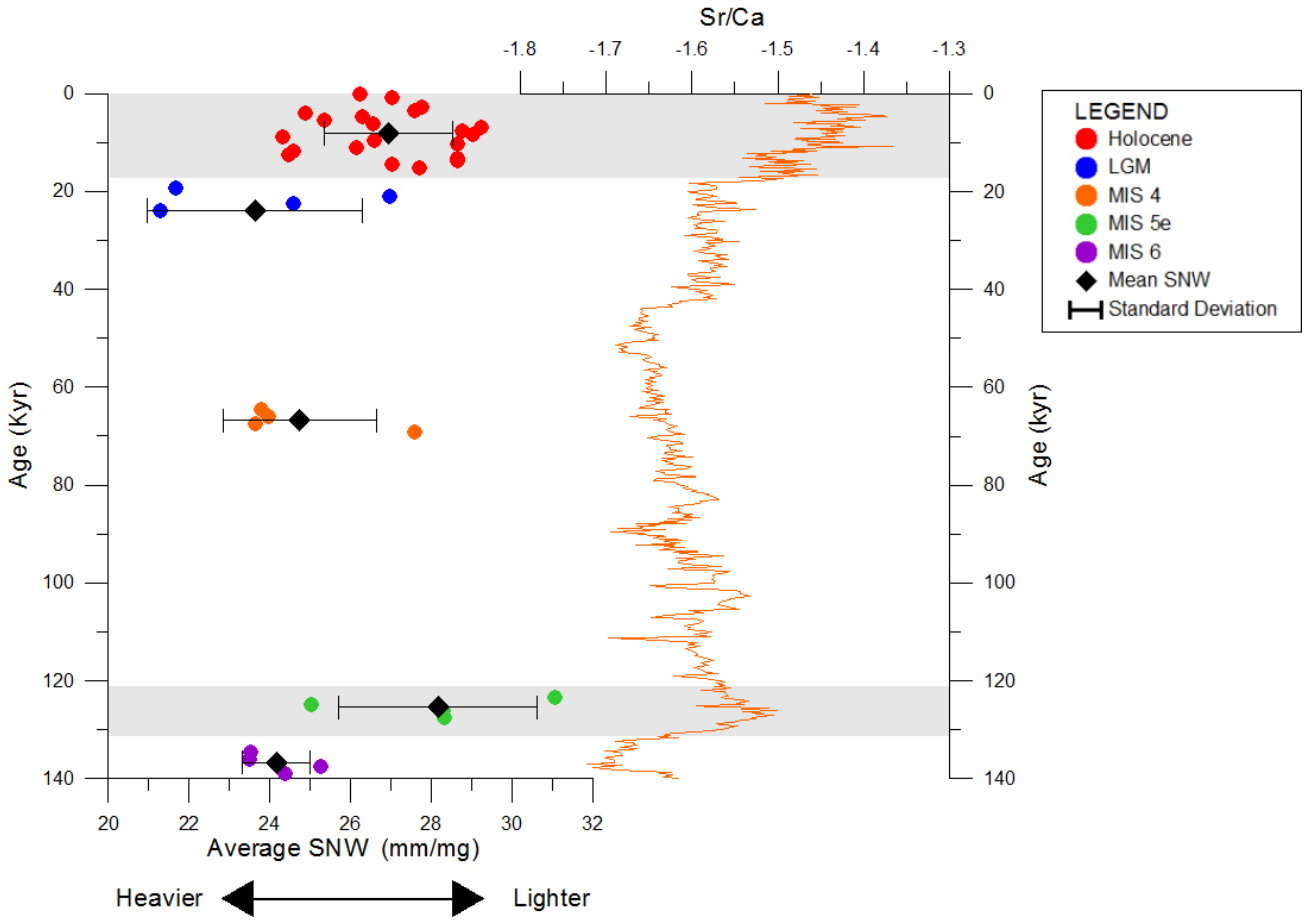

Fig 16) Average (20 specimens per sample) size normalized weights +/- standard deviation for each period. On the right the bulk Sr/Ca curve from the XRF data is added. The grey areas denote increased values of Sr/Ca that correlate with the interglacial periods (MIS5e and Holocene).

The variability in SNW may be caused by either differences in calcite production (i.e. reduced in LGM, MIS4 and MIS6) or differences in post-mortem dissolution (i.e. enhanced in LGM and MIS6). In the case of post-mortem dissolution higher atmospheric carbon dioxide levels during interstadials causes the seawater carbonate chemistry to change according to several chemical reactions:

$$CO_{2(atmos)} \leftrightarrow CO_{2(aq)} + H_2O \leftrightarrow H_2CO_3 \leftrightarrow H^+ + HCO_3^- \leftrightarrow 2H^+ + CO_3^{2-}$$ (Doney et al., 2009)

As atmospheric carbon dioxide levels increased to around 230-280 ppm in the Holocene and to around 270ppm during MIS 5e (Petit et al., 1999) the pH of the oceans decreased, hence increasing dissolution rates of calcite. On the other hand, calcite production (calcification rates) is influenced by different parameters, the concentration of carbonate ions, SST and to a lesser extent salinity and nutrient availability (Marr et al., 2011). Higher values of atmospheric CO_2 in

warmer periods result in a decrease of carbonate ions and reduced calcification rates (Barker & Elderfield, 2002; Devilliers, 2005).

Since the SEM images (see figure 17) of several specimens from different timeperiods do not show clear dissolution features it is more probable that the variability of SNW is related to variability in calcite production.

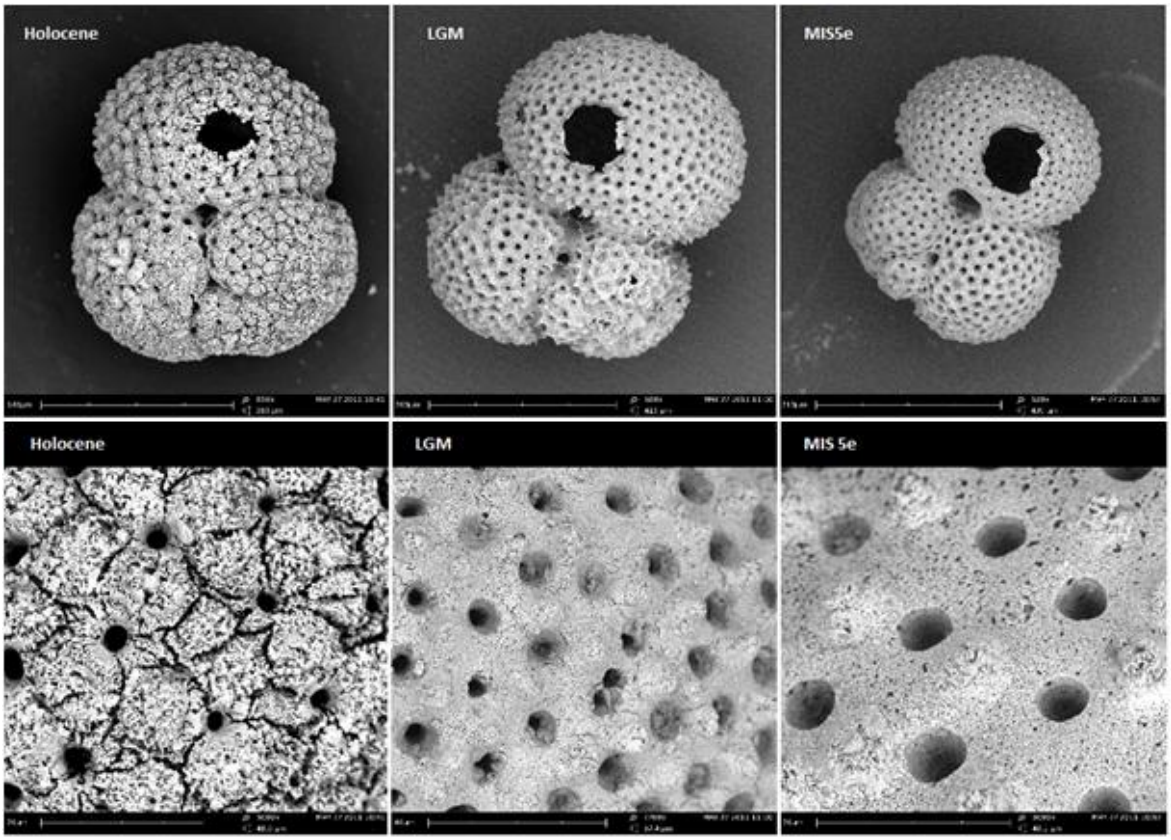

Fig 17) SEM images from several specimens of G. ruber *showing the different types of surface structures found within the core. Note that all surface types were found in each time interval and no relation was found between the time interval and surface structures.*

To analyze the relation between calcification and bulk Sr/Ca, the XRF Sr/Ca curve is compared to the SNW (figure 16). It is clear that during warmer periods MIS 5e and the Holocene correlate with increased values of Sr/Ca. If Sr/Ca is an indication of diagenesis, this suggests that during the Holocene and MIS 5e there was enhanced preservation and or less recrystallization. However, the Sr/Ca curve goes against the findings of Martin and colleagues (1999) in which Sr/Ca variability is mostly in line with changes in seawater Sr/Ca (the Sr/Ca should be greater during glacials due to greater Sr/Ca levels of seawater, see section 4.1). This suggests that variations of bulk Sr/Ca in this area are most likely due to another parameter. In this case, changes in temperature, which are higher during interglacials, could explain the higher Sr/Ca values.

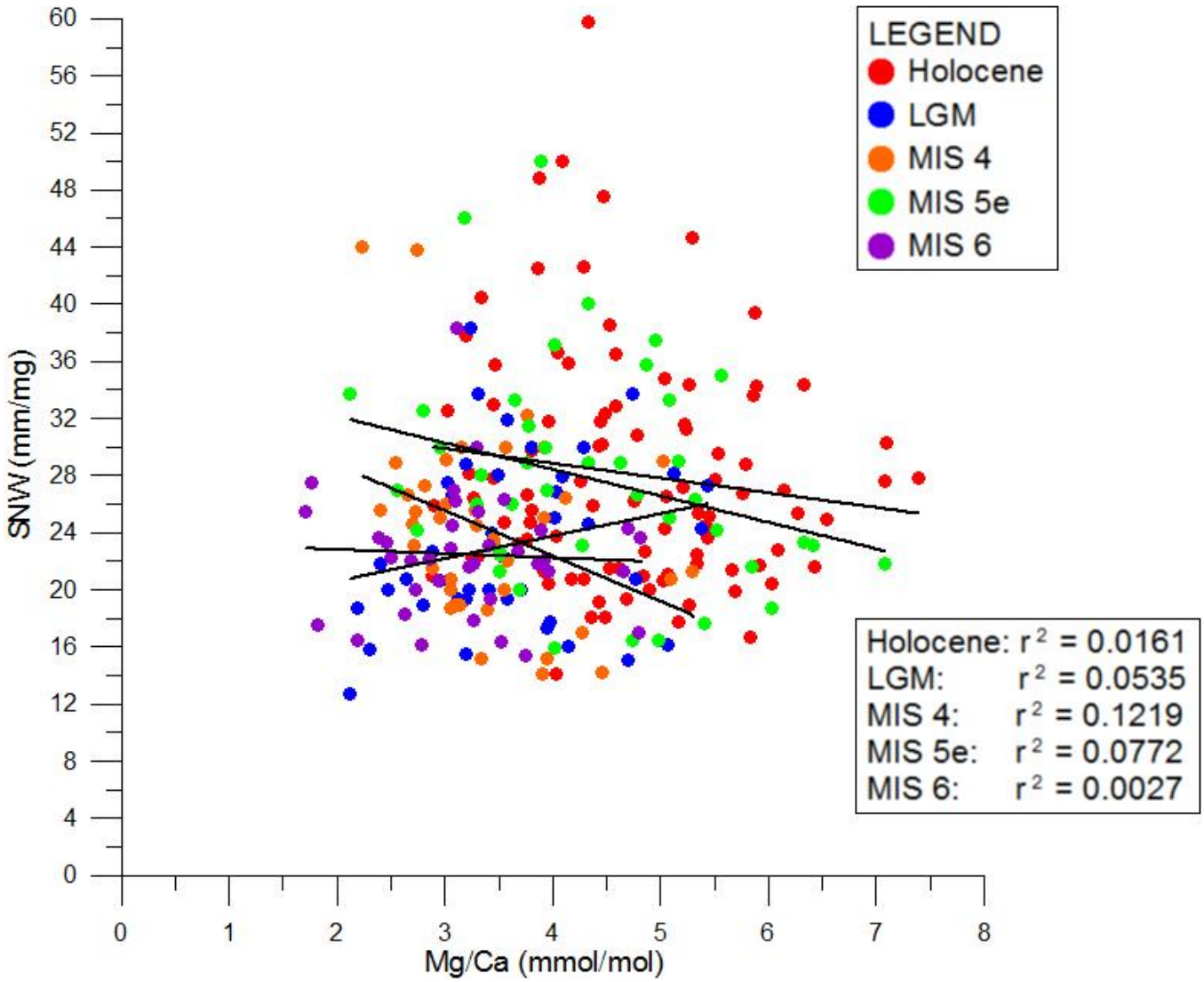

Fig 18) Relation between SNW and Mg/Ca ratios is very small, with r^2 equal to 0.0048 for all specimens. The individual R^2 per interval is shown on the right. The timeslices to which the specimens belong are depicted in different colors.

It is also important to see if the SNW is correlated to the Mg/Ca ratios in order to exclude the possibility that the reconstructed temperatures are influenced by production and or dissolution effects. Figure 18 shows that there is no significant correlation between Mg/Ca and SNW (see also figure C in appendix for total Mg/Ca - SNW trend), suggesting that SST is not directly responsible for the variability in shell thickness (i.e. SNW).

4.3. Mg/Ca measurements: INATEX-08

Obtained Mg/Ca (and thereby the reconstructed seawater temperatures) show a relatively large variability within and between timeslices (figure 19). Average Mg/Ca and reconstructed temperatures are comparable to previously published values. The variability in Mg/Ca and temperatures, however, differs between periods, with largest spread during the Holocene and MIS5.

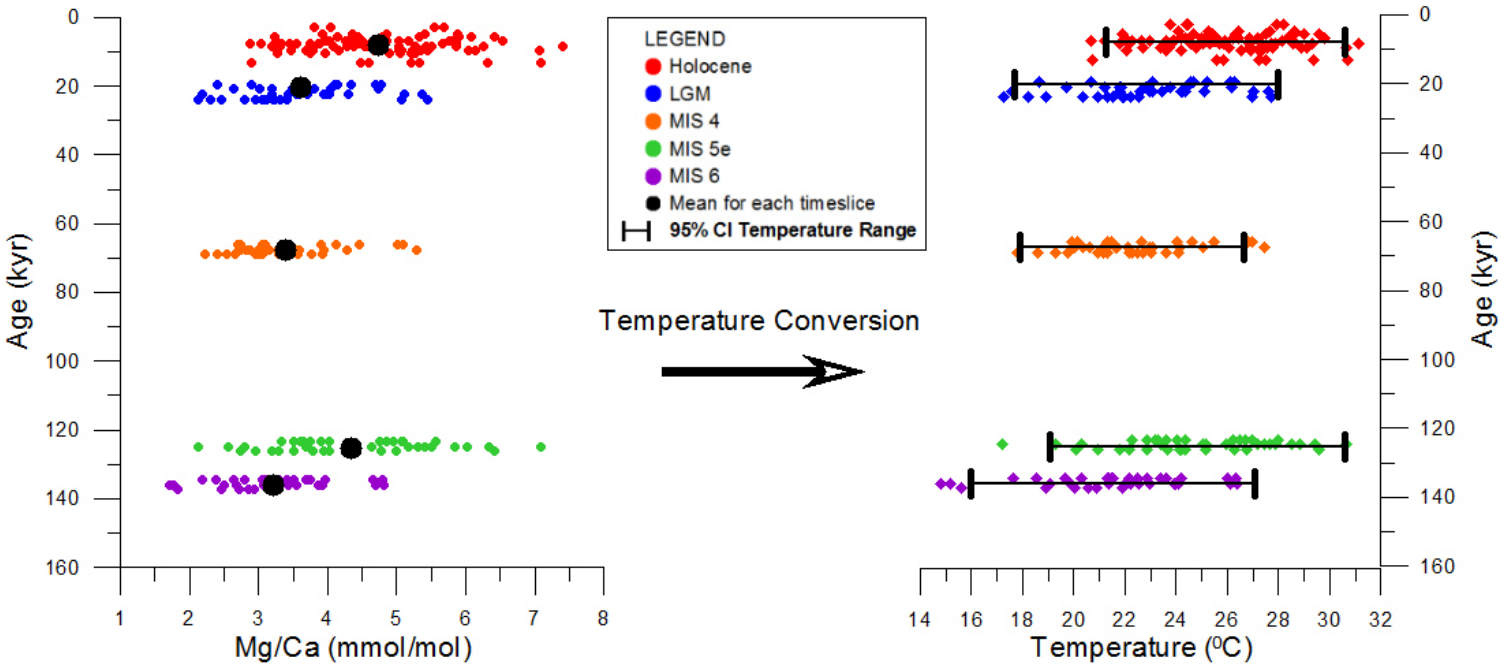

Fig 19) Left the Mg/Ca results for the different timeslices. The mean Mg/Ca ratio per timeslice is added as a black circle within the cloud of data of each timeslice. Note that the width (left to right) of the data shows the range of the Mg/Ca ratios for every timeslice. On the right the range of temperatures for every timeslice along with the 95% confidence interval (see below) for the temperature range are shown. The Holocene and MIS 5e timeslices clearly exhibit higher temperatures than the others.

To convert calcitic Mg/Ca into temperatures the formula for *G. ruber* from Anand et al. (2003) is used;

$$T = (1/0.09)*(LN(Mg/Ca)/0.449)$$

The reconstructed temperatures (figure 19) show that maximum temperatures of the Holocene (red) and MIS event 5e (green) exceed the maximum temperatures of the other timeslices; LGM, MIS 4 and MIS 6. Since the Holocene and MIS 5e are indeed warm periods and the other timeslices are colder periods, these results are a confirmation of previous expectations. Furthermore, the LGM and Holocene average temperatures differ by approximately 3 ºC.

Temperature range of reconstructed SST´s for each period is variable. Colder periods appear to have smaller temperature ranges than the warmer periods (see table 3). Using the extreme values, temperature ranges in the Holocene and LGM do not differ (10.46ºC and 10.45 ºC, respectively). Since outliers may have a relatively large effect in determining the range in reconstructed temperatures, a Gaussian curve was fitted through all single-specimen reconstructed temperatures and the calculated σ was used to estimate and standardize the variability in reconstructed temperatures for each period (figure 20).

Timeslice	Average T [=(LN(P2/0.449)/0.09)]	T range of actual data	95% confidence interval T range	Sample size per timeslice
Holocene	25.93	10.46036	9.316742	93
LGM	22.84	10.45698	10.30505	41
MIS 4	22.26	9.632018	8.739013	39
MIS 5e	24.84	13.43662	11.54283	42
MIS 6	21.54	11.54586	11.10218	37

Table 3) A summary of the average temperatures derived using Mg/Ca from LA-ICP-MS data, the temperature ranges and sample size per timeslice for INATEX 08

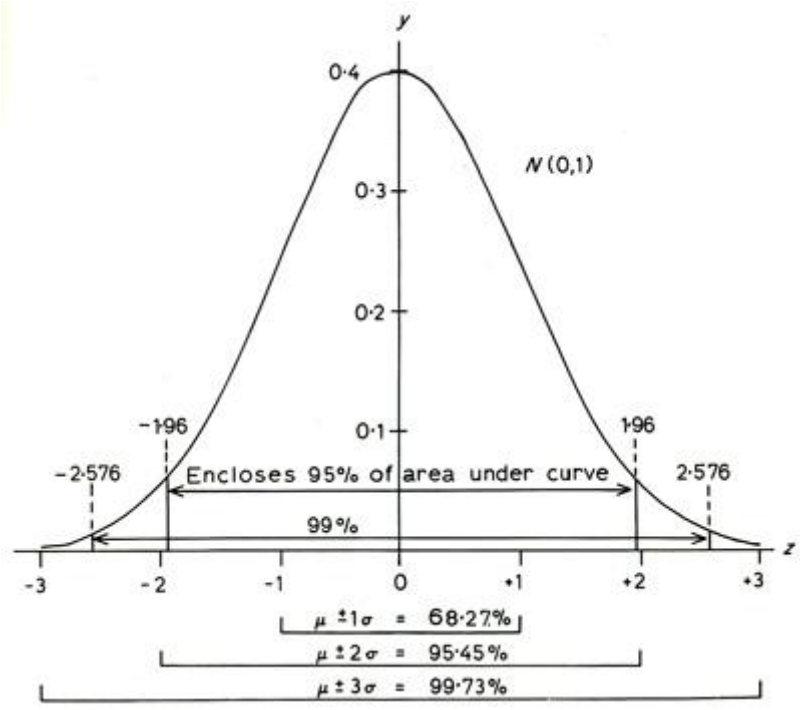

Fig 20) Gaussian distribution with the confidence intervals for 95% and 99% and their corresponding z values, used to estimate the variability in temperatures from normally distributed single-specimen derived Mg/Ca (modified from http://www4.nau.edu/microanalysis/microprobe-sem/statistics.html).

In order to minimize the effect of outliers and to standardize estimations of the variability, Temperature data is presented by means of histograms with Gaussian curves added to them (see figure 21). From these one can calculate the 95% interval boundaries by using the formula:

$Z = \mu \pm 1.96 * \sigma$

Where μ is the sample mean, σ is the sample standard deviation and ± 1.96 are the z values that correspond to a 95% confidence interval. The derived temperature ranges using the 95% confidence interval are also given in table 3.

The corrected minimum and maximum temperature limits show that temperature variability in the Holocene is smaller than in the LGM. Temperature variability in MIS 5e remains the largest, the colder episodes (MIS 4 and MIS 6) display considerably smaller temperature ranges than MIS 5e.

Furthermore, the histograms show that the peak of the Gaussian curves shifts from about 26 ºC in the Holocene to about 23 ºC in the LGM. In addition there seem to be multiple frequency peaks for the LGM, MIS 5e and MIS 6. These peaks may be the result of sediment displacement, in which case older and younger sediments (and foraminifera) are mixed. This sediment displacement may be caused by bioturbation, erosion due to changing sealevels or storm bed erosion. By looking at the XRF image scans it is safe to rule out bioturbation for the LGM since the sediments are very finely laminated at the corresponding depth, but at the depth corresponding to MIS 5e and MIS 6 the sediments are not laminated and are lighter colored, which may indicate oxygenation by bioturbation. The cause may also lie in the lifecycle of the foraminifera themselves, different water column depth (0-50m) or currents may also cause deviations in temperatures recorded by the foraminifera.

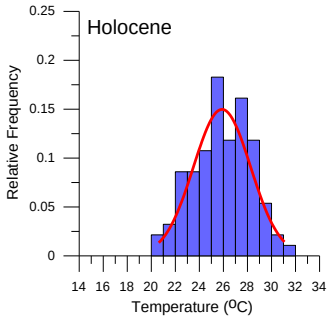

Fig 21) Histograms (A-E) illustrating the relative frequency of SST of each timeslice. Added to each histogram is a normal Gaussian distribution.

A) Holocene histogram, with an average of 25.93 ºC

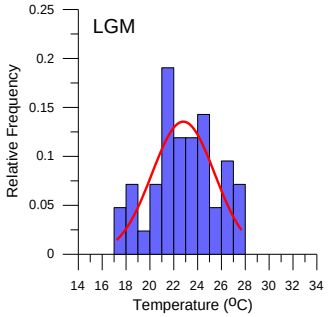

B) LGM histogram, with an average of 22.84 ºC

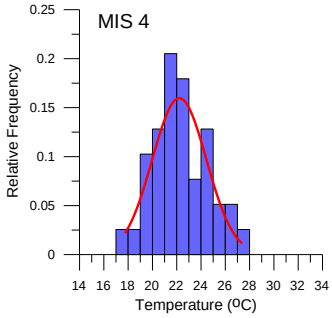

C) MIS 4 histogram, with an average of 22.26 ºC

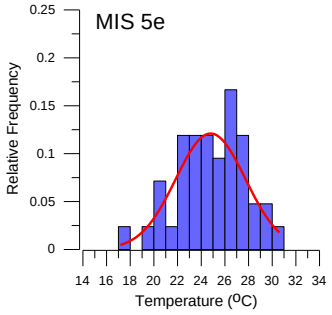

D) MIS 5e histogram, with an average of 24.84 ºC

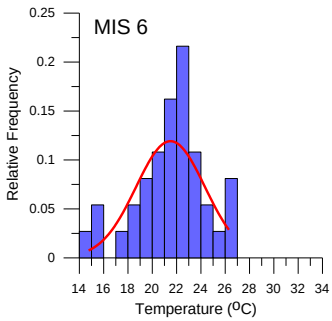

E) MIS 6 histogram, with an average of 21.54 ºC

4.4. Comparison of XRF scanning data

It is of interest to see how precession-forced proxies of the Northern cores compare to those of the Southern cores. The precessional signal of Zr/Rb, Fe/Ca and Br/Al ratios are compared for all cores. In the case of Zr/Rb the southernmost core shows a clear precessional signal, whereas the northern cores do not (see figure 22). The Zr/Rb curve for NIOP 905 does not have a clear resolution and the Zr/Rb curve of NIOP 478 does not show a precessional signal. Suggesting that Zr/Rb cannot be used as a comparative proxy that shows similar variability in the North and South Arabian Sea.

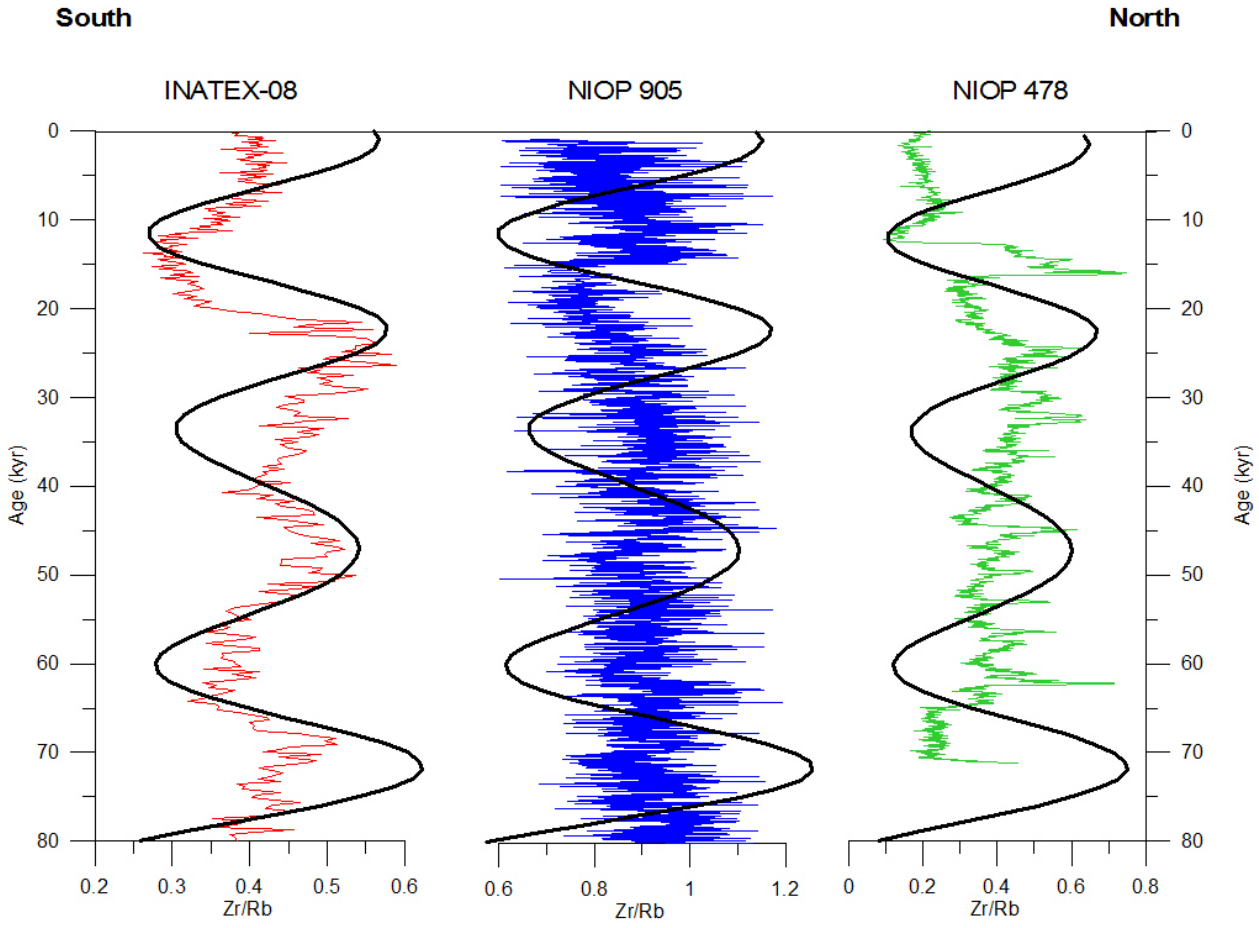

Fig 22) The Zr/Rb ratios for cores INATEX-08, NIOP 905 and NIOP 478. The precession curve in black (Laskar, 1990) is also shown in each of the cores.

A comparison between Fe/Ca and Br/Al of all cores (INATEX-08, NIOP 905, NIOP 463 and NIOP 478) shows that these can also not be used to show similar variability (figures A and B in Appendix). The lack of a common proxy showing similar variability in the Northern and Southern Arabian Sea suggests that different processes occur in the North and South Arabian Sea. There could be a difference in upwelling system and or wind system. The Br/Al sediment record of core INATEX-08 does not show obvious precession variations since, in the Northern

Arabian Sea, increased marine productivity is induced by the North east wind systems of the winter monsoon. Subsequently, periods of increased upwelling activity result in increased marine-organic carbon and Br concretions in marine sediments form this region (Ziegler et al., 2009). Contrary to the Northern Arabian Sea there is no distinct seasonal upwelling offshore Tanzania which can be related to the winter or summer monsoon wind system.

4.5. Comparison of Temperature data

To analyze temperature ranges and averages of INATEX-08 compare to Northern cores a comparison is made with data from previous studies. To analyze differences between proxy-derived and directly measured temperatures, coretop temperatures are first compared to present-day temperatures (derived from the World Ocean Atlas, 2009). In the table below annual and seasonal (April-June and January-March) temperatures at 0 and at 50m for each core are summarized. Core NIOP 463 is excluded from this section since no temperature is reconstructed from that core.

Phase	INATEX 08		NIOP 905		NIOP 478		NIOP 463	
	Depth = 0m	Depth = 50m	Depth = 0m	Depth = 50m	Depth = 0m	Depth = 50m	Depth = 0m	Depth = 50m
Annual Mean	27.3	26.2	26.1	24.6	26.6	23.4	26.8	24.2
SW (April-June) monsoon	27.8	26.6	27.9	26.3	27.6	23.4	27.6	23.4
NE (Jan-March) Monsoon	29.0	27.0	26.3	25.8	23.8	23.4	24.4	23.8

Table 4) Summary of the mean annual, SW monsoon and NE monsoon sea surface temperatures for depth 0m and at depth 50m below the surface(World Ocean Atlas 2009, On-line version at http://odv.awi.de/en/data/ocean/world_ocean_atlas_2009/).

In table 5 temperature data, methods and ages are shown for each core. The Holocene average temperature from INATEX-08 is 25.93ºC which is approximately one degree lower than the annual mean recorded recently at a depth of 0m (27.3ºC) and about the same as the annual mean at a depth of 50m (26.2ºC). Since no coretop temperature is measured it logical that the Holocene average differs from present day values.

Core NIOP 905 has coretop temperature data from different methods. The U^{k}_{37} coretop temperature has a value of 26.3ºC, whereas the TEX_{86} method gives a value of 25.7ºC. Compared to the annual mean of 26.1ºC both methods appear to be reliable tools to reconstruct mean sea surface temperature. Ganssen et al. (2010) applied the Mg/Ca method to core 905 and found an average temperature of 25.2ºC for the Holocene, about one degree less than the annual mean in the present at 0m. This deviation could be due to the fact that this is only an average Holocene temperature not a coretop average.

On the other hand for core NIOP 478 the coretop temperature, derived by the U^{k}_{37} method, is 26.8ºC as compared to an annual mean 26.6ºC.

		INATEX 08	NIOP 905			NIOP 478
Method		Mg/Ca	Uk37	TEX86	Mg/Ca	Uk37
Source		This study	Huguet et al., 2006	Huguet et al., 2006	Ganssen et al., 2010	De Nooijer, unpublished data
Average Temperature	coretop	-	26.3	25.7	-	26.8
	Holocene	25.93	25.7	29.0	25.2	25.97
	LGM	22.84	25.5	22.5	23.2	21.7
	MIS 4	22.26	-	-	-	21.6-23
	MIS 5e	24.84	-	-	-	-
	MIS 6	21.54	-	-	-	-
Temperature Range	Holocene	9.316	26.5-25 for last 23kyrs	28-30	13.1	24.5-27.11 for last 12kyrs
	LGM	10.305	-	22-23	10.6	21.67-24.17
	MIS 4	8.739	-	-	-	-
	MIS 5e	11.542	-	-	-	-
	MIS 6	11.102	-	-	-	-

Table 5) Summary of the average temperatures and temperature ranges derived for each core from different studies and methods.

Furthermore, one can compare the temperatures for different timeperiods between the cores (table 5). The focus lies upon the Holocene and LGM timeperiods and their difference. The Northern-most core, NIOP 478 has an average temperature of 25.97ºC (U^k_{37}) in the Holocene. NIOP 905 has average Holocene temperatures of 25.7ºC (U^k_{37}), 29.0ºC (TEX_{86}) and 25.2ºC (Mg/Ca). Looking only at the U^k_{37} temperatures, 25.97ºC (NIOP 478) and 25.7 ºC (NIOP 905), there is a difference of about 0.3ºC between the northernmost core and the central core. INATEX-08, the southernmost core has an average value of 25.93ºC for the Holocene, warmer than NIOP 905 and similar to NIOP 478. For the LGM, NIOP 478 has an average temperature of 21.7 ºC, NIOP 905 has average temperatures of 25.5ºC (U^k_{37}), 22.5ºC (TEX_{86}) and 23.2ºC (Mg/Ca), and INATEX-08 has an average temperature of 22.84ºC. The Northern-most core, NIOP 478 shows the coldest glacial temperature, INATEX-08 has a higher temperature by 1.1ºC. This data is summarized in figure 23.

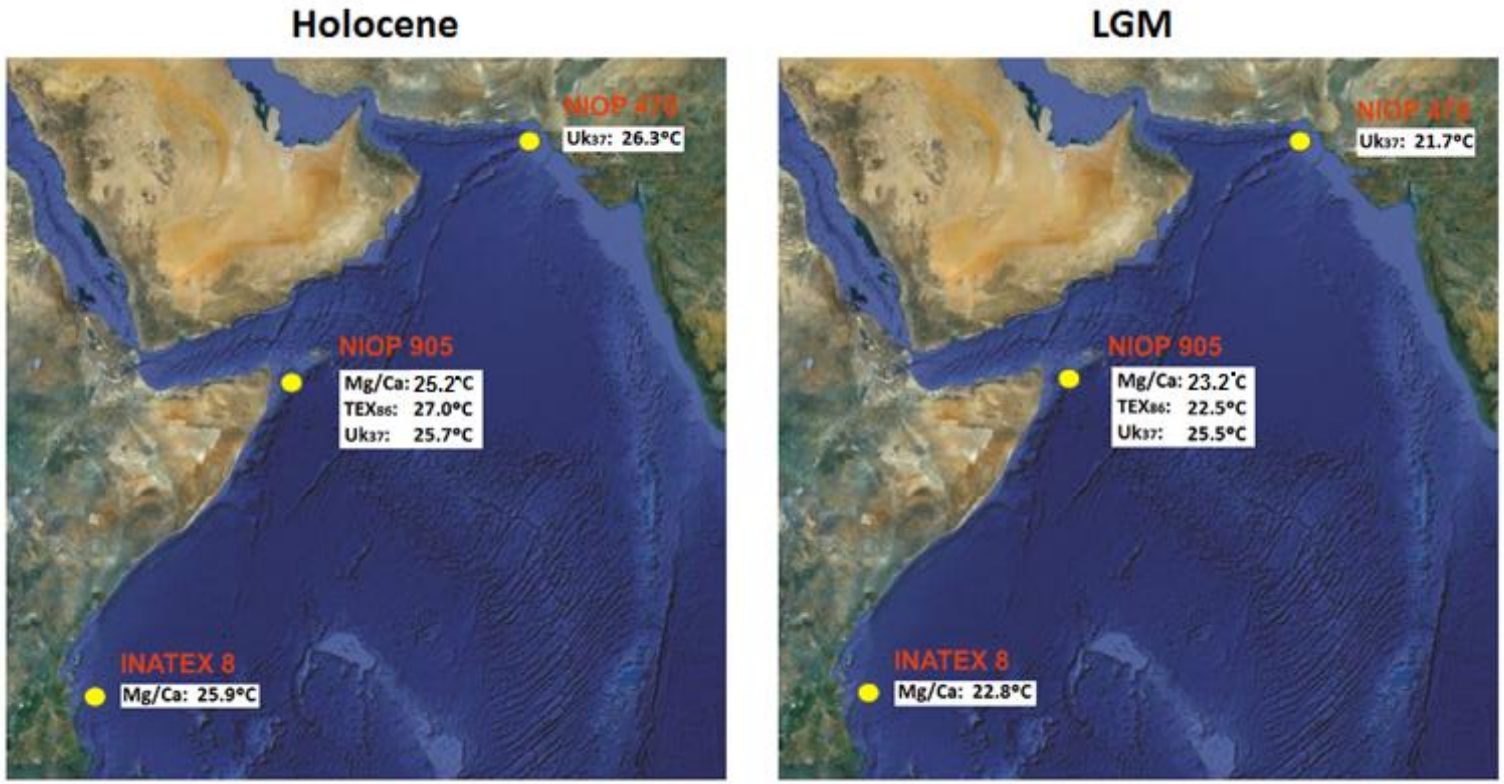

Fig 23) Comparison of the Holocene versus LGM sea surface temperatures for the different cores.

For NIOP 478 the average temperature increases from 21.7ºC during the LGM to 25.97ºC in the Holocene, comprising a difference of 4.3ºC. For NIOP 905 the difference between the LGM and the Holocene is 0.2ºC using the U^k_{37} method, 4.5ºC using the TEX_{86} method and 2.0ºC using the Mg/Ca method. For INATEX-08 this difference is 3.01ºC (figure 24). The LGM-Holocene temperature difference of 4.3ºC is greater in the north (NIOP 478) compared to the south; 3.01ºC (INATEX-08). TEX_{86} shows the largest difference, with warmer average temperature during the interglacial compared to the other proxies, and colder average temperature during the glacial (see red symbols of core NIOP 905). This large deviation of TEX_{86} from the other proxies could be related to a shift in the blooming season of the Crenarcheota (blooming in the summer during interglacials and in the winter during glacials) or due to change in depth habitat (deeper during glacial periods) or a combination of both. This needs to be further investigated. Looking at the Mg/Ca proxies only, it is seen that the LGM-Holocene difference is approximately the same with a slightly larger difference for INATEX-08 and colder temperatures for NIOP 478.

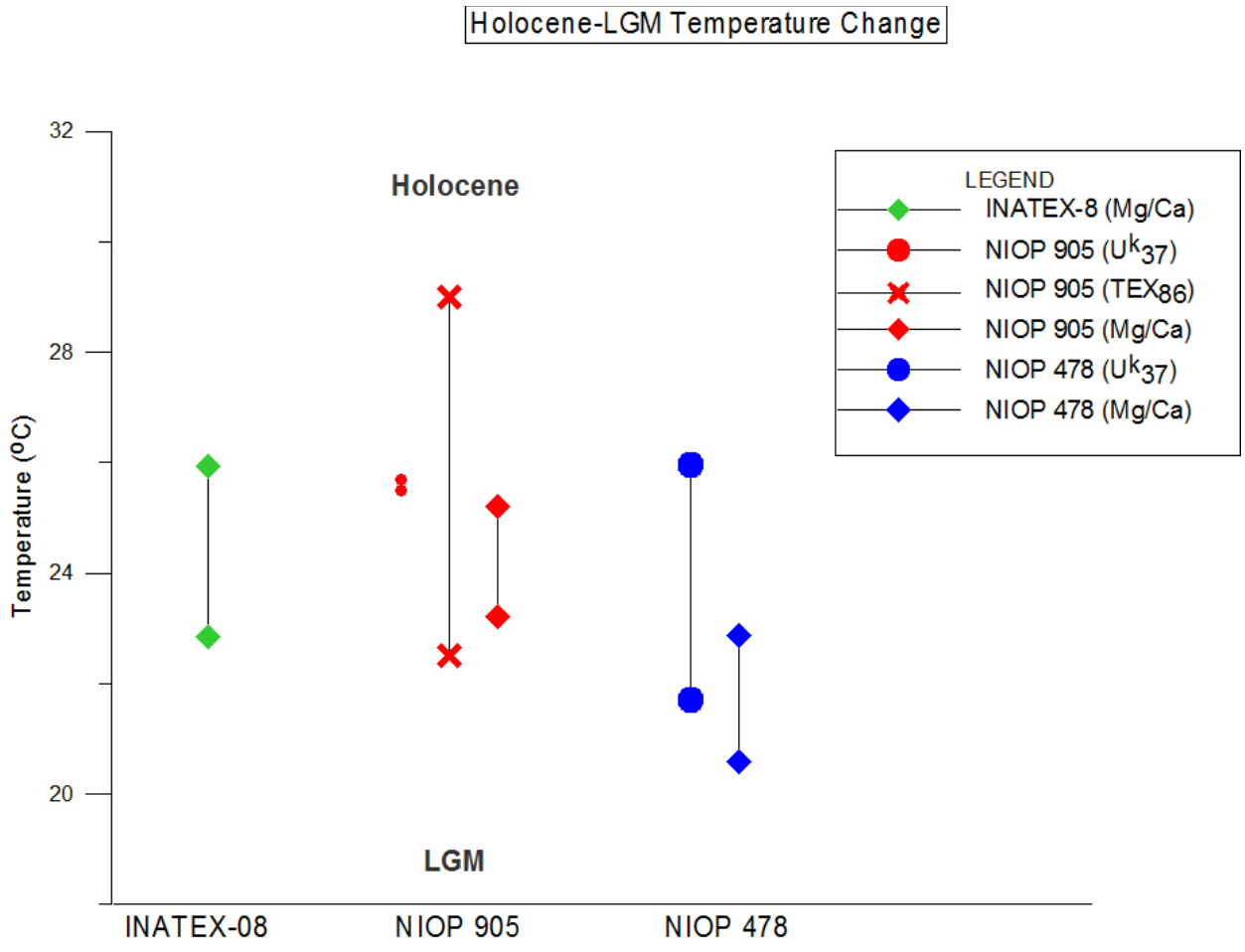

Fig 24) A comparison of the temperature difference between the LGM and the Holocene for the different cores, using the average values.

During the Holocene, temperature ranges become larger (for the Mg/Ca proxy) as one moves from the South to the North (see figure 25). The temperature range for NIOP 478 is the largest (~15 to ~29ºC). The lower end of this range is much below the minimum temperatures seen in the Northern Arabian Sea today. A very small sample size (27 specimens of *G.ruber*) was used to reconstruct the SST range for NIOP 478, hence this range may not be reliable. The TEX_{86} shows higher SST values than the Mg/Ca SST range and the U^k_{37} SST range, it is possible that TEX_{86} is not able to record intra-annual changes as well as Mg/Ca.

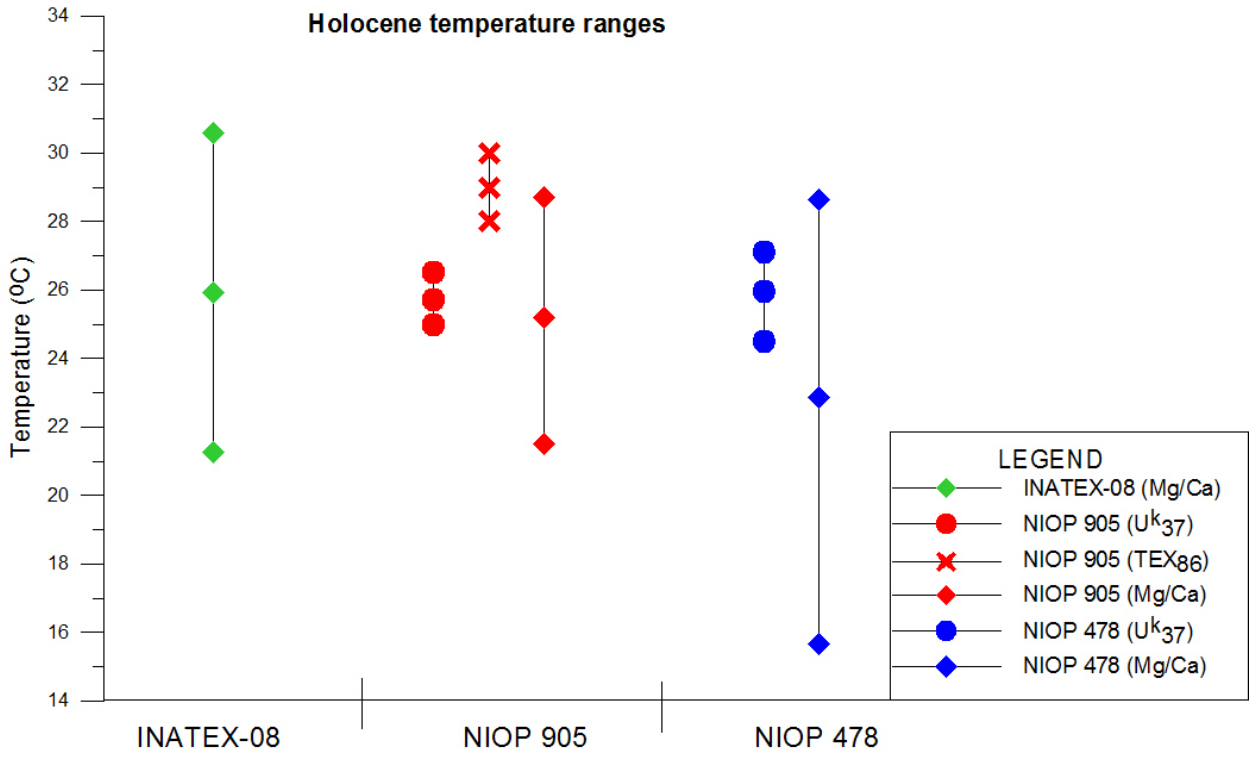

Fig 25) A comparison of the different Temperature ranges during the Holocene found by different methods for all cores. INATEX-08 range is from this study, NIOP 905 U^k_{37} and TEX_{86} temperature range is from Huguet et al. (2007) and NIOP 478 U^k_{37} temperature range is from De Nooijer (unpublished).

5. Conclusions

This study provides results from different data. The XRF scanning data shows 1) Strongly reduced lithogenic concentrations during MIS 6 and slightly reduced concentrations during MIS 4 and the LGM, 2) The last deglacial (around 12kyrs) shows the strongest increase in lithogenic material and highest lithogenic concentrations, 3) Zr/Rb ratios show a strong increase of the coarse-grained lithogenic fraction during the deglacial (12kyrs) and 4) The high Zr/Rb ratios during the LGM, MIS 4 and MIS 6 suggest a reduction of the lithogenic sand fraction during glacial periods.

The relative lithogenic variations indicated by the Ti/Ca ratio and variations of the lithogenic grain-size suggest that higher lithogenic concentrations are related with an increase the lithogenic sand fraction. Since the XRF results indicate times of increased coarser terrigenous material at ~130 and 12kyrs, which correspond to a transition interval between a glacial and an interglacial (between MIS6 and MIS 5e and between the LGM and the Holocene), these shifts are probably due to changes in sealevel.

Also, it is seen that lithogenic grainsize minima correlate to obliquity maxima at around 170 kyrs and 130 kyrs (which is the deglacial period after MIS 6). From around 70kyrs the lithogenic grainsize is dominated by the precession cycle. Zr/Rb, Fe/Ca and Br/Al do not vary in similar ways (precession signal) in the South and North Arabian Sea suggesting different processes are playing a role in the South and North.

Furthermore, a comparison between SST proxies of Southern and Northern cores shows that 1) the LGM-Holocene difference is approximately the same for all cores with a slightly larger difference for INATEX-08 and colder temperatures for NIOP 478, 2) TEX_{86} shows the largest difference, with warmer average temperature during the interglacial compared to the other proxies, and colder average temperature during the glacial, 3) The Mg/Ca SST ranges of the Holocene become larger as one moves from the South to the North with the temperature range for NIOP 478 being the largest, 4) The TEX_{86} shows higher SST values than the Mg/Ca SST range and the U^{k}_{37} SST range, it is possible that TEX_{86} is not able to record seasonality changes as well as Mg/Ca.

Concluding, further research can be performed on multiple fronts. To begin with performing an oxygen isotope analysis on the same specimens used to quantify the temperature ranges (INATEX8) may provide a more reliable reconstruction of seasonality. An additional planktonic foraminifera that flourishes during upwelling, such as *G.bulloides*, may also improve the reconstruction of seasonal differences.

It is also of importance to investigate the differences in SST recorded by different proxies for future SST reconstructions. Especially TEX_{86} SST does not seem to overlap Mg/Ca and U^{k}_{37} ranges, and the average values appear to be higher during interglacials and lower during glacial.

Next, the SNW can be investigated as a proxy for pH or carbonate ion concentration, since the SNW is higher in warmer periods suggesting lighter shells in warmer periods. This can be investigated by conducting a live culture experiment in which the influence of temperature and pH on shell weight are tested.

This study focused upon the LGM-Holocene transition. Since SST, SNW and XRF data is available for more timeslices (MIS4, MIS 5e and MIS 6) one could investigate these intervals with that of other cores.

Another interesting study is investigating the role of obliquity and precession on the grainsize and terrigenous material proxies (XRF) for INATEX 8. How does obliquity and or precession influence the monsoon system and how is this recorded in the sediments.

Finally one can perform a chemical analysis and SEM analysis on the sediments of INATEX-08 in order to find the sources of terrigenous input, which may help explain why there is a bimodal grainsize distribution and from where (what distance) the monsoon winds transport this material (indication of monsoon strength).

7. References

Anand, P., H. Elderfield & M.H. Conte. (2003), Calibration of Mg/Ca thermometry in planktonic foraminifera from a sediment trap time series. Paleoceanography 18(2), pp.28-31.

Anand, P., D. Kroon, A.D. Singh et al. (2008), Coupled sea surface temperature–seawater d18O reconstructions in the arabian sea at the millennial scale for the last 35 ka. Paleoceanography 23

Arz, H.W., J. Pätzold & G. Wefer. (1998), Correlated millennial-scale changes in surface hydrography and terrigenous sediment yield inferred from last-glacial marine deposits off northeastern brazil. Quaternary Research 50(2), pp.157-166.

Baker, P.A., J.M. Gieskes & H. Elderfield. (1982), Diagenesis of carbonates in deep-sea sediments; evidence from Sr/Ca ratios and interstitial dissolved sr (super 2) data. Journal of Sedimentary Research 52(1), pp.71.

Barker, S., M. Greaves & H. Elderfield. (2003), A study of cleaning procedures used for foraminiferal Mg/Ca paleothermometry. Geochemistry Geophysics Geosystems 4(9), pp.8407.

Beer, C.J., R. Schiebel & P.A. Wilson. (2010), Testing planktic foraminiferal shell weight as a surface water [CO32-] proxy using plankton net samples. Geology 38(2), pp.103.

Böning, P., E. Bard & J. Rose. (2007), Toward direct, micron-scale XRF elemental maps and quantitative profiles of wet marine sediments. Geochemistry Geophysics Geosystems 8(5), pp.Q05004.

Burns, S.J., D. Fleitmann, A. Matter et al. (2003), Indian ocean climate and an absolute chronology over Dansgaard/Oeschger events 9 to 13. Science 301(5638), pp.1365.

Burns, S.J., D. Fleitmann, M. Mudelsee et al. (2002), A 780-year annually resolved record of indian ocean monsoon precipitation from a speleothem from south oman. Journal of Geophysical Research 107(D20), pp.4434.

Chowdary, J.S., C. Gnanaseelan, S.K. Sinha et al. (2006), A study on the variability of atmospheric and oceanic processes over the arabian sea during contrasting monsoons. Meteorology and Atmospheric Physics 94(1), pp.65-85.

Clark, C.O., J.E. Cole & P.J. Webster. (2000), Indian ocean SST and indian summer rainfall: Predictive relationships and their decadal variability. Journal of Climate 13, pp.14.

Clemens, S., W. Prell, D. Murray et al. (1991), Forcing mechanisms of the indian ocean monsoon. Nature 353(6346), pp.720-725.

Clemens, S.C. (1998), Dust response to seasonal atmospheric forcing: Proxy evaluation and calibration. Paleoceanography 13(5), pp.471-490.

Clemens, S.C. & W.L. Prell. (2003), A 350,000 year summer-monsoon multi-proxy stack from the owen ridge, northern arabian sea. Marine Geology 201(1-3), pp.35-51.

Clemens, S.C., W.L. Prell, Y. Sun et al. (2008), Southern hemisphere forcing of pliocene δ18O and the evolution of indo-asian monsoons. Paleoceanography 23(4)

Croudace, I.W., A. Rindby & G. Rothwell. (2006), ITRAX: Description and evaluation of a new multi-function X-ray core scanner. New techniques in sediment core analysis 267, pp.51–63.

Dekens, P.S., D.W. Lea, D.K. Pak et al. (2002), Core top calibration of Mg/Ca in tropical foraminifera: Refining paleotemperature estimation. Geochem.Geophys.Geosyst 3(4), pp.1022.

Den Dulk, M., G.J. Reichart, S. Van Heyst et al. (2000), Benthic foraminifera as proxies of organic matter flux and bottom water oxygenation? A case history from the northern arabian sea. Palaeogeography, Palaeoclimatology, Palaeoecology 161(3-4), pp.337-359.

Doney, S.C., V.J. Fabry, R.A. Feely et al. (2009), Ocean acidification: The other CO2 problem. Annual Review of Marine Science 1, pp.169-192.

Eggins, S., P. De Deckker & J. Marshall. (2003), Mg/Ca variation in planktonic foraminifera tests: Implications for reconstructing palaeo-seawater temperature and habitat migration. Earth and Planetary Science Letters 212(3-4), pp.291-306.

Elderfield, H. & G. Ganssen. (2000), Past temperature and δ18O of surface ocean waters inferred from foraminiferal Mg/Ca ratios. Nature 405(6785), pp.442-445.

Emeis, K.C., D.M. Anderson, H. Doose et al. (1995), Sea-surface temperatures and the history of monsoon upwelling in the northwest arabian sea during the last 500,000 years. Quaternary Research 43(3), pp.355-361.

Erez, J. (2003), The source of ions for biomineralization in foraminifera and their implications for paleoceanographic proxies. Reviews in mineralogy and geochemistry 54(1), pp.115.

Fleitmann, D., S.J. Burns, M. Mudelsee et al. (2003), Holocene forcing of the indian monsoon recorded in a stalagmite from southern oman. Science 300(5626), pp.1737.

Ganssen, G. et al. (2010), Quantifying sea surface temperature ranges of the Arabian Sea for the past 20 000 years. Climate of the Past Discussions 6(6), pp. 2795-2814.

Hastenrath, S. & L. Greischar. (1993), The monsoonal heat budget of the hydrosphere-atmosphere system in the indian ocean sector. Journal of Geophysical Research 98(C4), pp.6869-6881.

Hastenrath, S., A. Nicklis & L. Greischar. (1993), Atmospheric-hydrospheric mechanisms of climate anomalies in the western equatorial indian ocean. Journal of Geophysical Research 98(C11), pp.20219.

Hinte van, J.E., T.C.E. van Weering & S.R. Troelstra. (1995), Tracing a seasonal upwelling : report on two cruises of RV Tyro to the NW Indian Ocean in 1992 and 1993. Cruise reports vol.4, Leiden : National Museum of Natural History

Huguet, C., J.H. Kim, J.S.S. Damsté & S. Schouten.(2006), Reconstruction of sea surface temperature variations in the Arabian Sea over the last 23 kyr using organic proxies (TEX86 and K´37 U). Paleoceanography, 21

Ivanochko, T.S., R.S. Ganeshram, G.J.A. Brummer et al. (2005), Variations in tropical convection as an amplifier of global climate change at the millennial scale. Earth and Planetary Science Letters 235(1-2), pp.302-314.

Jansen, J.H.F., S.J. Van der Gaast, B. Koster et al. (1998), CORTEX, a shipboard XRF-scanner for element analyses in split sediment cores. Marine Geology 151(1), pp.143-153.

Jung, S.J.A., G.R. Davies, G. Ganssen et al. (2002), Decadal-centennial scale monsoon variations in the arabian sea during the early holocene. Geochemistry Geophysics Geosystems 3(10), pp.1060.

Jung, S.J.A., G.R. Davies, G.M. Ganssen et al. (2004), Synchronous holocene sea surface temperature and rainfall variations in the asian monsoon system. Quaternary Science Reviews 23(20-22), pp.2207-2218.

Jung, S.J.A., D. Kroon, G. Ganssen et al. (2009), Enhanced arabian sea intermediate water flow during glacial north atlantic cold phases. Earth and Planetary Science Letters 280(1-4), pp.220-228.

Kalnicky, D.J. & R. Singhvi. (2001), Field portable XRF analysis of environmental samples. Journal of hazardous materials 83(1-2), pp.93-122.

Lea, D.W., T.A. Mashiotta & H.J. Spero. (1999), Controls on magnesium and strontium uptake in planktonic foraminifera determined by live culturing. Geochimica et Cosmochimica Acta 63(16), pp.2369-2379.

Lisiecki, L.E. & M.E. Raymo. (2005), A plio-pleistocene stack of 57 globally distributed benthic δ 18 O records. Paleoceanography 20, pp.522–533.

Liu, L., J. Chen, J. Ji et al. (2004), Comparison of paleoclimatic change from Zr/Rb ratios in chinese loess with marine isotope records over the 2.6–1.2 ma BP interval. Geophysical Research Letters 31(15), pp.L15204.

Liu, W.T. (1994), Evaporation and solar irradiance as regulators of sea surface temperature in annual and interrannual changes.

Liu, X., Z. Liu, J.E. Kutzbach et al. (2006), Hemispheric insolation forcing of the indian ocean and asian monsoon: Local versus remote impacts*. Journal of Climate 19(23), pp.6195-6208.

Loschnigg, J. & P.J. Webster. (2010), A coupled Ocean–Atmosphere system of SST modulation for the indian ocean*.

Marr, J.P., J.A. Baker, L. Carter et al. (2011), Ecological and temperature controls on Mg/Ca ratios of globigerina bulloides from the southwest pacific ocean. Paleoceanography 26(2), pp.PA2209.

Martin, P., D. Lea, T. Mashiotta et al. (1999), Variation of foraminiferal Sr/Ca over quaternary glacial-interglacial cycles: Evidence for changes in mean ocean Sr/Ca? Geochemistry Geophysics Geosystems 1(12), pp.1004-1019.

Martrat, B., J.O. Grimalt, N.J. Shackleton et al. (2007), Four climate cycles of recurring deep and surface water destabilizations on the iberian margin. Science 317(5837), pp.502.

Matthewson, A.P., G.B. Shimmield, D. Kroon et al. (1995), A 300 kyr high-resolution aridity record of the north african continent. Paleoceanography 10(3), pp.677-692.

McClanahan, T.R. (1988), Seasonality in east africa's coastal waters. Marine ecology progress series.Oldendorf 44(2), pp.191-199.

McDermott, F., D.P. Mattey & C. Hawkesworth. (2001), Science 294(5545), pp.1328.

Naidu, P.D. & P. Govil. New evidence on the sequence of deglacial warming in the tropical indian ocean. Journal of Quaternary Science

Neff, U., S.J. Burns, A. Mangini et al. (2001), Strong coherence between solar variability and the monsoon in oman between 9 and 6 kyr ago. Nature 411(6835), pp.290-293.

Nürnberg, D. (1995), Magnesium in tests of neogloboquadrina pachyderma sinistral from high northern and southern latitudes. The Journal of Foraminiferal Research 25(4), pp.350.

Nürnberg, D., J. Bijma & C. Hemleben. (1996), Assessing the reliability of magnesium in foraminiferal calcite as a proxy for water mass temperatures. Geochimica et Cosmochimica Acta 60(5), pp.803-814.

Paillard, D., L. Labeyrie & P. Yiou. (1996), Analyseries 1.0: A macintosh software for the analysis of geographical time-series. Eos 77, pp.379.

Pearce, N.J.G., Perkins, W.T., Westgate, J.A., Gorton, M.P., Jackson, S.E., Neal, C.R. and Chenery, S.P., (1997), A compilation of new and published major and minor trace element data for NIST SRM 610 and 612 certified glass reference material. *Geostandards Newsletter :The Journal of Geostandards and Geoanalysis, 21, 115-144.)* .

Peeters, F.J.C., G.J.A. Brummer & G. Ganssen. (2002), The effect of upwelling on the distribution and stable isotope composition of globigerina bulloides and globigerinoides ruber (planktic foraminifera) in modern surface waters of the NW arabian sea. Global and Planetary Change 34(3-4), pp.269-291.

Prins, M.A., G. Postma & G.J. Weltje. (2000), Controls on terrigenous sediment supply to the arabian sea during the late quaternary: The makran continental slope. Marine Geology 169(3-4), pp.351-371.

Rampen, S.W., S. Schouten, E. Koning et al. (2008), A 90 kyr upwelling record from the northwestern indian ocean using a novel long-chain diol index. Earth and Planetary Science Letters 276(1-2), pp.207-213.

Reichart, G.J., H. Brinkhuis, F. Huiskamp et al. (2004), Hyperstratification following glacial overturning events in the northern arabian sea. Paleoceanography 19(2)

Reichart, G.J., M. den Dulk, H.J. Visser et al. (1997), Palaeogeography, Palaeoclimatology, Palaeoecology 134(1-4), pp.149-169.

Reichart, G.J., F. Jorissen, P. Anschutz et al. (2003), Single foraminiferal test chemistry records the marine environment. Geology 31(4), pp.355.

Reichart, G.J., L.J. Lourens & W.J. Zachariasse. (1998), Temporal variability in the northern arabian sea oxygen minimum zone (OMZ) during the last 225,000 years. Paleoceanography 13, pp.607-621.

Richmond, M. (1997). A guide to the seashores of eastern africa and the western indian ocean islands

Richter, T.O., S. van der Gaast, B. Koster et al. (2006), The avaatech XRF core scanner: Technical description and applications to NE atlantic sediments. Geological Society London Special Publications 267(1), pp.39.

Rohling, E.J., Q.S. Liu, A.P. Roberts et al. (2009), Controls on the east asian monsoon during the last glacial cycle, based on comparison between hulu cave and polar ice-core records. Quaternary Science Reviews 28(27-28), pp.3291-3302.

Rosenthal, Y., E.A. Boyle & N. Slowey. (1997), Temperature control on the incorporation of magnesium, strontium, fluorine, and cadmium into benthic foraminiferal shells from little bahama bank: Prospects for thermocline paleoceanography. Geochimica et Cosmochimica Acta 61(17), pp.3633-3643.

Rosenthal, Y., G.P. Lohmann, K.C. Lohmann et al. (2000), Incorporation and preservation of mg in globigerinoides sacculifer: Implications for reconstructing the temperature and 18O/16O of seawater. Paleoceanography 15(1), pp.135-145.

Rostek, F., E. Bard, L. Beaufort et al. (1997), Sea surface temperature and productivity records for the past 240 kyr in the arabian sea. Deep Sea Research Part II: Topical Studies in Oceanography 44(6-7), pp.1461-1480.

Sadekov, A., S.M. Eggins, P. De Deckker et al. (2008), Uncertainties in seawater thermometry deriving from intratest and intertest Mg/Ca variability in globigerinoides ruber. Paleoceanography 23(1)

Sadekov, A., S.M. Eggins, P. De Deckker et al. (2009), Surface and subsurface seawater temperature reconstruction using Mg/Ca microanalysis of planktonic foraminifera globigerinoides ruber, globigerinoides sacculifer, and pulleniatina obliquiloculata. Paleoceanography 24(3)

Sadekov, A.Y., S.M. Eggins & P. De Deckker. (2005), Characterization of Mg/Ca distributions in planktonic foraminifera species by electron microprobe mapping. Geochem.Geophys.Geosyst 6, pp.Q12P06.

Saher, M.H. (2007), History of the indian monsoon: Implications of sea surface temperatures in the arabian sea over terminations I and II.

Saher, M.H., F. Rostek, S.J.A. Jung et al. (2009), Western arabian sea SST during the penultimate interglacial: A comparison of U37K′ and Mg/Ca paleothermometry. Paleoceanography 24(2)

Schouten, S. & E.C. Hopmans. (2002), Distributional variations in marine crenarchaeotal membrane lipids: A new tool for reconstructing ancient sea water temperatures? Earth and Planetary Science Letters 204(1-2), pp.265-274.

Shackleton, N.J., M.F. Sánchez-Goņi, D. Pailler et al. (2003), Marine isotope substage 5e and the eemian interglacial. Global and Planetary Change 36(3), pp.151-155.

Shukla, J. (1975), Effect of arabian sea-surface temperature anomaly on indian summer monsoon: A numerical experiment with the GFDL model. J.Atmos.Sci 32(3), pp.503–511.

Sinha, J.S.C.C.G.S.K. & B. Thompson. (2006), A study on the variability of atmospheric and oceanic processes over the arabian sea during contrasting monsoons. Meteorology and Atmospheric Physics 94(1-4)

Swallow, J.C., F. Schott & M. Fieux. (1991), Structure and transport of the east african coastal current. Journal of Geophysical Research 96(C12), pp.22245-22,257.

Takahashi, T., S.C. Sutherland, C. Sweeney et al. (2002), Global sea-air CO2 flux based on climatological surface ocean pCO2, and seasonal biological and temperature effects. Deep Sea Research Part II: Topical Studies in Oceanography 49(9-10), pp.1601-1622.

Thompson, P.R., A.W.H. Bé, J.C. Duplessy et al. (1979), Disappearance of pink-pigmented globigerinoides ruber at 120,000 yr BP in the indian and pacific oceans.

Tjallingii, R., U. Röhl, M. Kölling et al. (2007), Influence of the water content on X-ray fluorescence core-scanning measurements in soft marine sediments. Geochemistry, Geophysics, Geosystems 8(2), pp.1–12.

van der Weijden, C.H., G. Reichart & B.J.H. van Os. (2006), Sedimentary trace element records over the last 200 kyr from within and below the northern arabian sea oxygen minimum zone. Marine Geology 231(1-4), pp.69-88. DOI: DOI: 10.1016/j.margeo.2006.05.013

Wang, B. & Q. Ding. (2006), Changes in global monsoon precipitation over the past 56 years. Geophys.Res.Lett 33, pp.L06711.

Webster, P.J. (1987), The elementary monsoon. Monsoons.Wiley, New York, pp.3–32.

Webster, P.J. (1994), The role of hydrological processes in ocean-atmosphere interactions. Reviews of Geophysics 32(4), pp.427-476.

Webster, P.J. & R. Tomas. (1998), Monsoons- processes, predictability, and the prospects for prediction. Journal of Geophysical Research 103(C7), pp.14451-14510.

Wit, J.C., G.-. Reichart, A Jung S.J. et al. (2010), Approaches to unravel seasonality in sea surface temperatures using paired single-specimen foraminiferal δ18O and Mg/Ca analyses. Paleoceanography 25(4), pp.PA4220. DOI: 10.1029/2009PA001857

Xie, S.P., H. Annamalai, F.A. Schott et al. (2002), Structure and mechanisms of south indian ocean climate variability. Journal of Climate 15(8), pp.864-878.

Yanai, M. & T. Tomita. (2010), Seasonal and interannual variability of atmospheric heat sources and moisture sinks as determined from NCEP–NCAR reanalysis.

Ziegler, M., T. Jilbert, G.J. de Lange et al. (2009), Bromine counts from XRF scanning as an estimate of the marine organic carbon content of sediment cores. Orbital forcing of the late Pleistocene boreal summer monsoon: Links to North Atlantic cold events and El Niño–Southern Oscillation, pp.19.

Ziegler, M., L. Lourens, E. Tuenter et al. (2010), High arabian sea productivity conditions during MIS 13–odd monsoon event or intensified overturning circulation at the end of the mid-pleistocene transition? Climate of the Past 6, pp.63-76.

WOCE Global Hydrographic Climatology, Gouretski & Koltermann 2004 and Ocean data View, available at http://odv.awi.de/

8. Appendix

Figure A

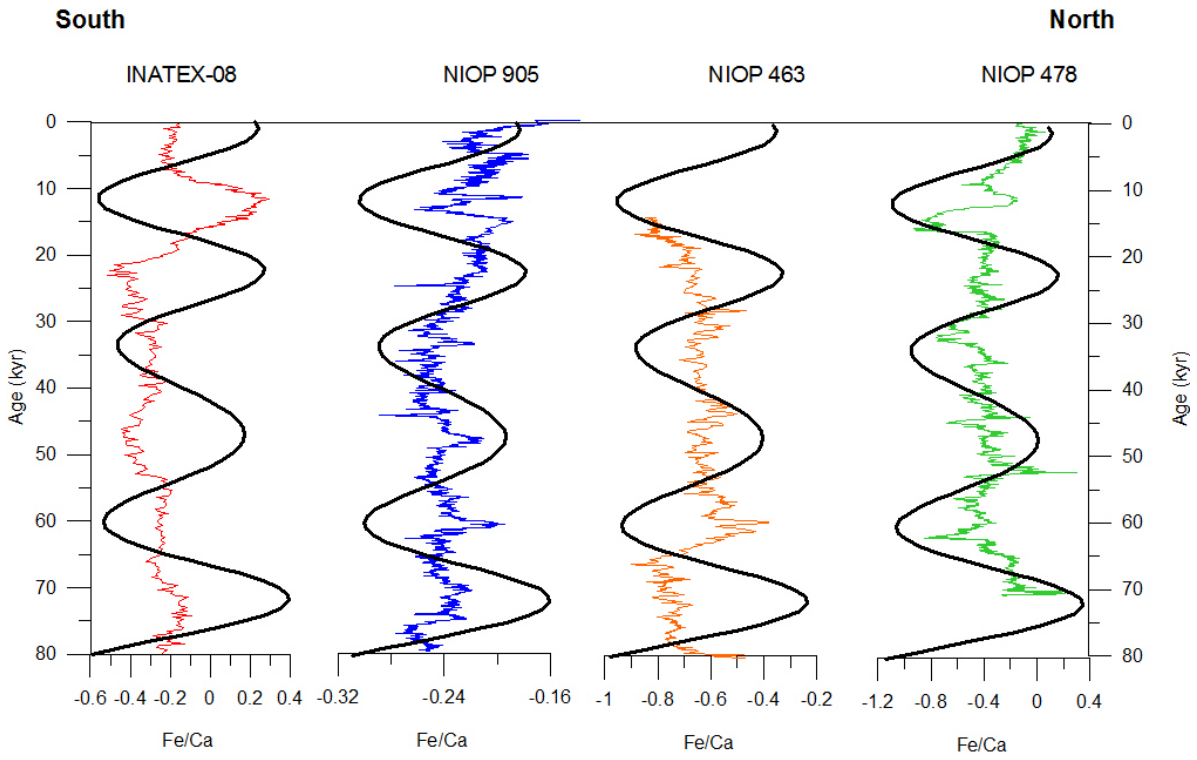

Figure B

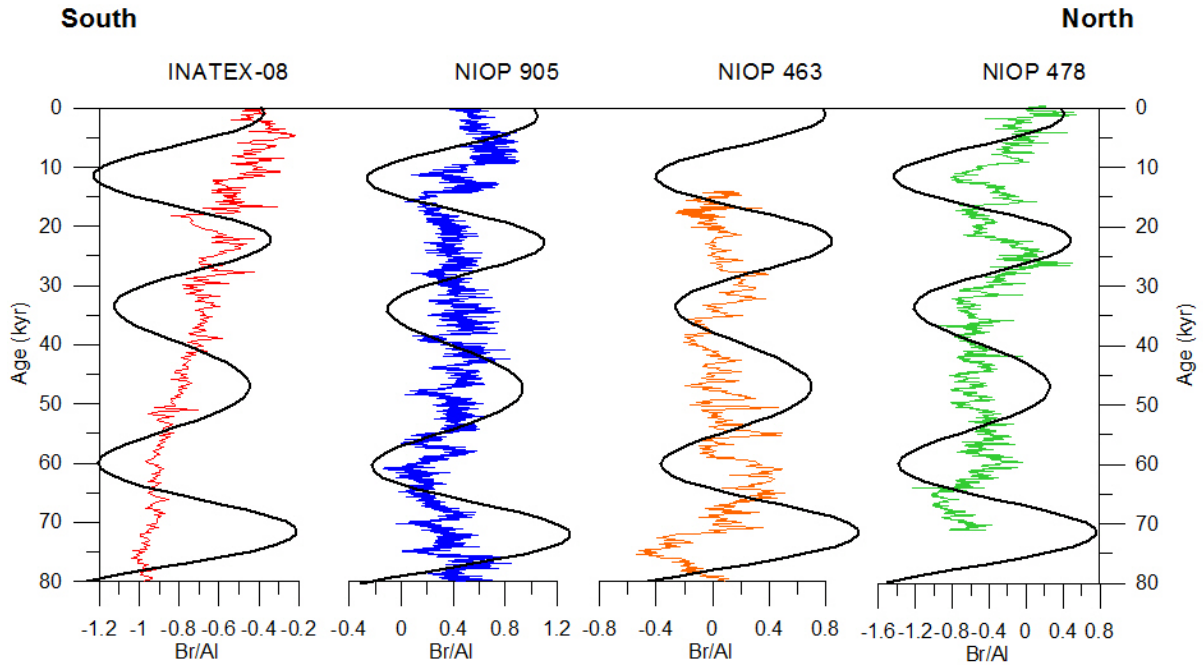

Figure C

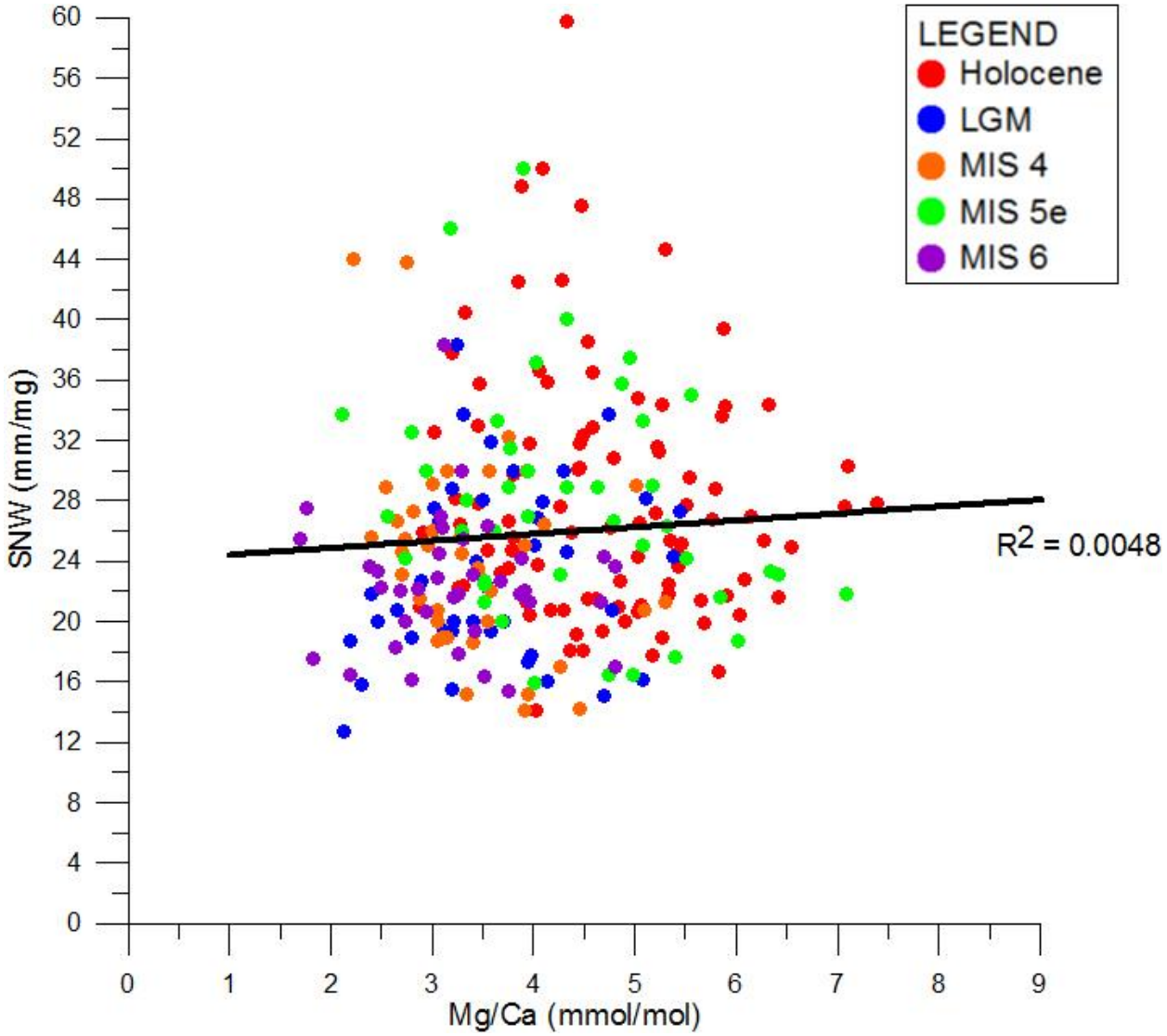
LEGEND
Holocene
LGM
MIS 4
MIS 5e
MIS 6
SNW (mm/mg)
Mg/Ca (mmol/mol)
R2 = 0.0048
0
4
8
12
16
20
24
28
32
36
40
44
48
52
56
60
0
1
2
3
4
5
6
7
8
9